



**Politecnico
di Torino**

Politecnico di Torino

DIPARTIMENTO DI INGEGNERIA ENERGETICA

Corso di Laurea magistrale in Ingegneria Energetica e Nucleare - Renewable energy Systems

TESI DI LAUREA MAGISTRALE

Computational thermal-fluid dynamic and thermo-mechanic analysis of the Neutralizer of the DTT NBI

Candidato:

Silvia Pierri

Matricola S303628

Relatore:

Prof Andrea Zappatore

Correlatore:

Prof. Roberto Bonifetto

Anno Accademico 2023–2024

Contents

1	Abstract	3
2	Introduction	4
	2.0.1 Global Electrical Energy Overview	4
	2.0.2 Nuclear Fusion	5
	2.1 Nuclear fusion development	9
	2.2 Neutral Beam Injector	11
	2.3 DTT NBI design	15
	2.4 Aim of the work and methodology	19
3	Thermal-fluid dynamics evaluations	21
	3.1 Introduction	22
	3.1.1 physic continua	22
	3.2 Mesh characteristics	26
	3.2.1 Single LEE evaluation	26
	3.3 Neutralizer Design 1	36
	3.3.1 Geometry and heat loads	36
	3.3.2 Simulation and results	36
	3.4 Neutralizer Design 2	39
	3.4.1 Geometry and heat loads	39
	3.4.2 Simulation and results	41
	3.4.3 Summary of Design 2 thermal-fluid dynamics results . . .	48
	3.5 Neutralizer Design 3	51
	3.5.1 Geometry and heat loads	51
4	Thermomecanic evaluations	52
	4.1 Introduction	53
	4.1.1 Physics continua	53
	4.2 Mesh characteristic	56
	4.3 Panels and SFSS evaluations	57
	4.3.1 Panels	57
5	Conclusions	64

Acronyms

CAD Computer Aided Design. 16

CAE Computer Aided Engineering. 7

CSS Cylindrical Sawtooth Structure. 16, 35

DEMO DEMOnstration power plant. 11, 15

DTT Divertor Tokamak Test. 7, 11

IAPWS-IF97 International Association for the Properties of Water and Steam,
Industrial Formulation 1997. 20, 21

ITER International Thermonuclear Experimental Reactor. 11, 15

LEE Leading Edge Element. 18, 24, 28, 32, 33, 43, 45

NBI Neutral Beam Injector. 7, 15

RFX Reversed Field eXperiment. 7, 16

SFSS Stray Field Shielding System. 16, 17, 37, 43, 44

1 Abstract

In this thesis work, a thermal-fluid dynamic and thermo-mechanic assessment of the Neutral Beam Injector (NBI) system (together with its magnetic shield) of the Divertor Tokamak Test (DTT) Facility is presented; the NBI is currently being designed by RFX researchers. The neutralizer is subjected to high heat loads, coming from the Deuterium and Electron beams interacting with it; it is cooled by water flowing in dedicated pipes within its solid structure. The aim of the work is to compute the temperature distribution in the component (both solid and fluid domains); furthermore, the pressure drop of the neutralizer within its circuit is also evaluated. Different geometries and heat load are considered and compared, since the thesis work followed the evolution of the component design. Once the 3D geometry is properly discretized, numerical simulations have been carried out using the Finite Volume method, with Siemens Star CCM+ software. The same tool has been employed also to assess the component deformations due to the thermal expansion, through the finite element method. According to the results, all the major constraints in terms of maximum allowed pressure drop and hot spot temperature are satisfied.

2 Introduction

2.0.1 Global Electrical Energy Overview

Global consumption of electrical energy is really likely to increase in future (see the trend of figure 1) **tually nuclear fusion energy would have a great positive impact on one of the most important issues of our era.**

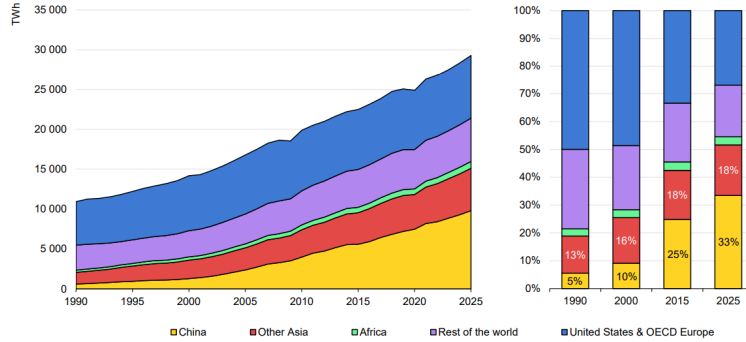


Figure 1: Evolution of global electricity demand by region (left) and regional shares (right), 1990-2025 [22].

In the IEA report in [22], which was published in 2023 and refers to 2022 situation, shows that by 2025 global demand of electrical energy will increase by 2 500 TWh from 2022 levels. This is related to the fact that developing countries are really energy demanding and they will increase consumptions in the future.

Share of the global electricity production, is shown in figure 2, nowadays, relies mainly for the biggest part from the fossil fuels, even if a considerable part is generated from renewable sources, more than one third of the gross electricity still depends on coal which is the fossil fuel which emits more CO_2 , furthermore another $\sim 10\%$ is produced by using nuclear power plants, which of course exploit fission technology.

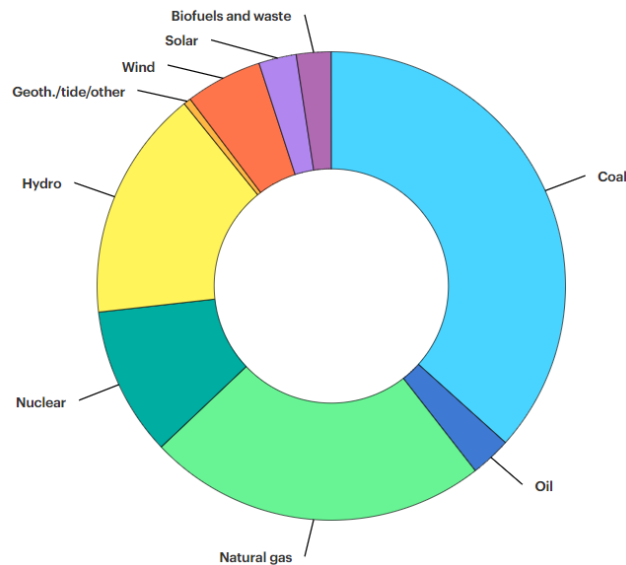


Figure 2: World gross electricity production by source, 2019 [21]

Fuels combustion emit polluting and greenhouse gases in the atmosphere. Greenhouse effect manifests as an increment of the average world temperature, and in the past ten years, the problem of climate change caused by anthropologic activities has become serious [25], that is why in the future it is foreseen to increase the share of energy coming from sustainable sources.

2.0.2 Nuclear Fusion

Nuclear fusion can be considered a sustainable source of energy, it is [13]:

- environment-friendly, since the product of the most promising fusion reaction (Deuterium and Tritium) is just Helium and Neutrons, with a proper choice of the materials employed the induced radioactivity in components will decay in short time if compared with fusion technology.
- intrinsically safe: fusion reaction automatically switches off in case of accidents or damages.
- sustainability and has secure supply: the fuel is widely available
- CO_2 -free: there's no production of greenhouse gases

Basic concepts When two atoms collide, a nuclear fusion reaction is happening and some energy is released. Nuclear fusion reactions power stars, like the Sun, in which the gravitational force and the temperature at the center of the star are so high that the fusion occurs naturally. Managing to achieve a way to reproduce this mechanism on earth would mean to obtain a lot of energy.

Nuclear Fusion Energy field, aims to exploit the fusion reaction that happens between two isotopes of Hydrogen in order to produce energy that, then would be converted into electricity. .

The exploited Hydrogen isotopes are Deuterium (D) and Tritium (T); Deuterium has just one neutron and Tritium has two, in Figure 3 there is a representation of their fusion reaction:

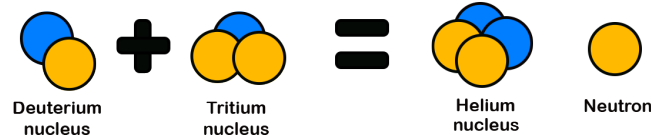


Figure 3: Nuclear Fusion Reaction Representation

As it is possible to see in the image above, the fusion products are a Helium nucleus (also called α particle) and a Neutron, each one carrying its own share of energy in form of kinetic energy.

But, where does this energy comes from? To explain this question, Nuclear binding energy has to be introduced, this is the minimum energy that is required to disassemble the nucleus of an atom into its constituent protons and neutrons ("nucleons"), inversely when the different parts of an atom nucleus aggregate to form it, there's a mass unbalance " Δm ", between the sum of the single nucleons one i.e. m_1 , and the one of the nucleus they will form: m_2 , $m_1 - m_2 = \Delta m > 0$. Δm , when the nucleons aggregate, is expelled in form of energy (following the Einstein's law $E = mc^2$), and its amount is just the nuclear binding energy. Since the energy used to separate D and T in their nucleons (D+T binding energy), is less than the one needed to, then, form the He^4 nucleus (He^4 binding energy), there is an excess which can be exploited, see figure 4:

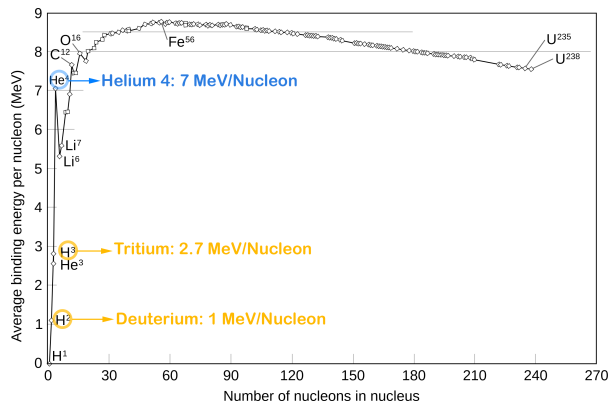


Figure 4: Nuclear binding energy [1]

It is possible to write:

$$\begin{array}{rclcl}
2 \cdot 1 \sim 2MeV & + & 3 \cdot 2.7 \sim 8MeV & \approx & 10MeV \\
\textit{Binding energy D nucleus} & & \textit{Binding energy T nucleus} & & \\
4 \cdot 7 \sim 28MeV & - & 10MeV & \approx & 18MeV \\
\textit{Binding energy He}^4\textit{nucleus} & & & & \textit{D - T Fusion Reaction energy}
\end{array}$$

The expelled energy, is distributed between the α particle and Neutron, inversely to their mass: $\sim 3MeV$ to the first and $\sim 14MeV$ to the second. The α particle energy is larger than the one needed to activate the D-T fusion reaction so, it in turn could fuel another one. The resulting neutron, since it doesn't feel the confinement magnetic field will exit the plasma and hit the walls of the reactor, transferring its energy, which is used to produce steam that then will expand in turbine producing electricity.

Concerning the fuel availability, as already anticipated, it is widely available:

Deuterium can be extracted from ocean water

Tritium will be breed, exploiting the from lithium present in the reactor itself.

All these reactions happend between atoms nuclei, i.e. atoms without the surrounding electrons, there are different ways to achieve a fusion reaction, it is possible to divide in two major types of fusion reactors:

Inertial confinement: which exploits lasers to compress a fuel filled target to let nuclei collide

Magnetic confinement: which uses heaters and magnets to create and confine plasma in which the fusion reactions will occur

Magnetic confinement The state of matter in which an atom nucleus detaches from its electrons is called plasma. To obtain the plasma, a lot of energy has to be provided to the D-T fuel. Plasma is extremely hot for example in ITER (whose story is descibrd in section 2.1) it is foreseen that the reached plasma temperatures will soar to between 150 and 300 million $^{\circ}C$, while in Sun the reached temperatures are around "just" 15 million $^{\circ}C$ [7]. Any material in contact with materials at this so high temperature, would melt, a solution, is to employ magnetic field to keep the plasma confined and trying to avoid contact with other materials as much as possible. There are two different technologies to achieve magnetic confinement:

The Tokamak configuration, where an electric current is induced in the plasma such that a poloidal magnetic confinement field is generated, a slightly more information is provided in section 2.3.

The Stellarator, in which the magnetic fields of its configuration are all generated from the outside by means of magnetic coils which have the characteristic of being very twisted to give the desired complex shape to optimize the confinement of the particles [10].

Although stellator has been the first configuration to be proposed in order to achieve magnetic plasma confinement, nowadays the research is focusing more on

tokamaks, this work actually is developed around this technology. In tokamaks, electricity is obtained by exploiting the neutrons which will hit the tokamak walls depositing their energy there in form of heat in the plasma facing components, heat that then will be harvested through a cooling fluid and used to make a steam turbine to rotate, and so, producing electricity as shown in figure 5:

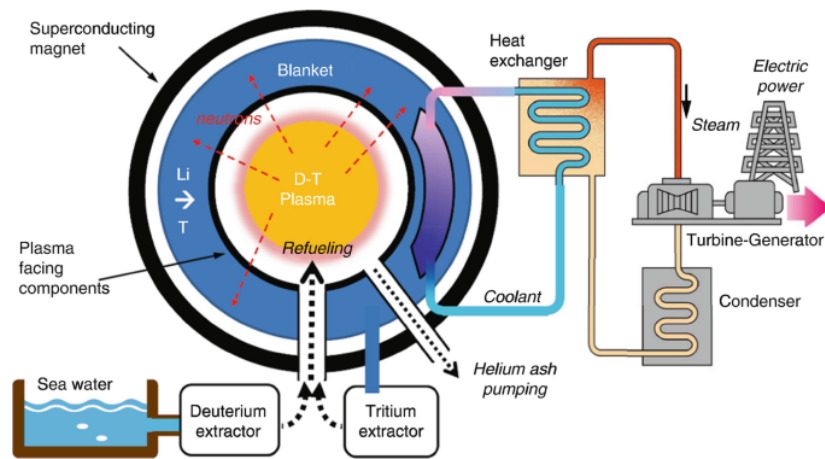


Figure 5: Overall tokamak system [38].

2.1 Nuclear fusion development

Fusion history starts when first fusion experiments were conducted in Cavendish laboratory, in Cambridge in 1930 while the magnetic confinement idea arose in 1938. In a first moment the main technology was the stellarators 1950-1965 but the results with this technology were not satisfying since the strong particle losses due field inhomogeneity. In 1951 Andrei Sakharof and Igor Tamm proposed a way to avoid drifts in plasma: the tokamak, in which the current would pass inside the plasma itself. In Geneva, in 1958 2nd Conference on Peaceful Uses of Atomic Energy United States, Soviet Union, and Europe agree to declassify fusion research and in the same year IAEA was founded in order to facilitate the international cooperation for nuclear fusion. From 1960 on fusion interested different experiments all around the world. In 1970 NBI and radio frequency heating systems were introduced [29]. In 1985 ITER was set in motion at the Geneva Superpower Summit. One year later the European Union (Euratom), Japan, the Soviet Union and the USA would jointly pursue the design for a large international fusion facility : ITER [9] whose objectives are to test the availability of essential technologies for a fusion reactor and also test components for future reactors like exhaust power and tritium breeding[27]

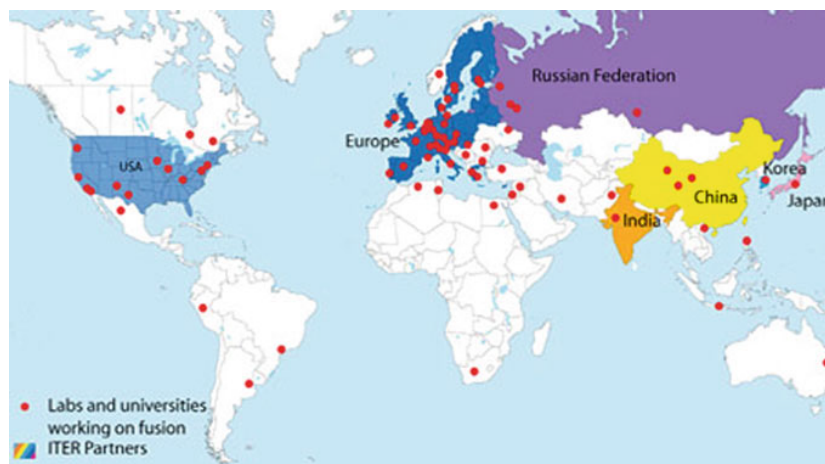


Figure 6: Countries and laboratories participating in the ITER project (from F4E)

With Eurofusion DEMO project, Magnetic confined Fusion power plant will be brought for the first time to an industry-driven and technology-driven level, it will be useful to demonstrate the technological aspects necessary to safely generating electricity consistently, and for regular, rapid, and reliable maintenance of the plant [15] DEMO will be operational around 20 years after high power burning plasmas are demonstrated in ITER [32], which is another plant being currently built in Cadarache (France), to assess the scientific and technological feasibility of fusion energy [12].

The point in which Fusion can be considered as a reliable source of energy, thus, is little bit far in future, but that point sooner or later will arrive, see figure 7.

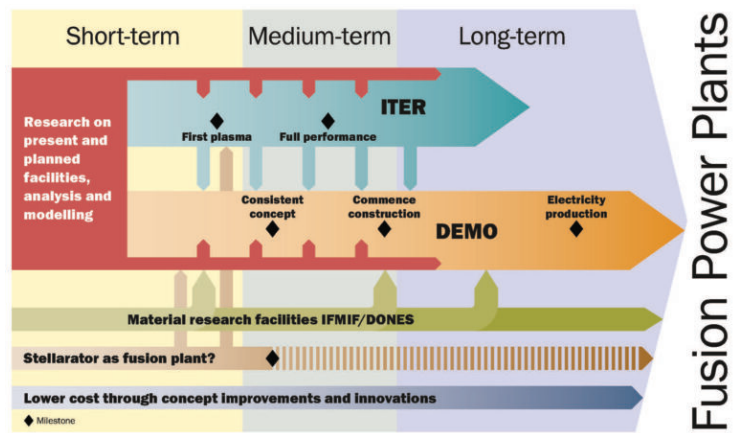


Figure 7: Nuclear Fusion Reactors Roadmap phases [32]

DTT, which will be built in Frascati, in Italy is a Tokamak in which scaled experiments will be useful to migrate from the today's proof-of-principle experiments to DEMO by bringing technological solutions to an appropriate level of maturity, in particular this project focuses main on the problem of power and particle exhaust since the solutions adopted for ITER could not be extrapolated for DEMO, so there will be the possibility to test different divertor magnetic configurations, liquid metals divertor targets and other possible solutions [13].

2.2 Neutral Beam Injector

Despite the heat generated due ohmic heating inside the plasma itself, there are two main methods envisaged for provide external heat to the fuel, in order to bring it at the temperatures at which it is self-sustained: the injection of energetic neutral beams and the resonant absorption of radio frequency electromagnetic waves (figure 8).

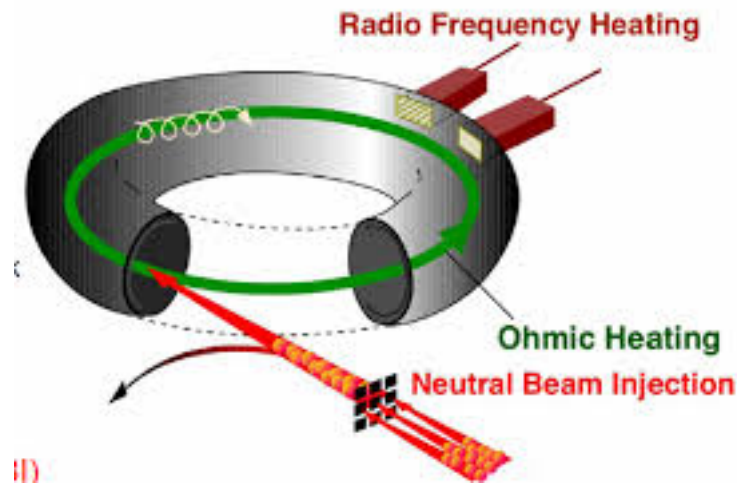


Figure 8: Plasma heating techniques in tokamaks [18].

why the NBI is needed Deuterium and tritium nuclei, repel each other since they have the same positive charge, this means that the cross section for the fusion is really small at low energies but it increases with energy. In fusion, a positive energy balance is possible if the fuel particles retain their energy and remain in the reacting region for a sufficient time. One of the methods of supplying the energy is to heat the deuterium-tritium fuel to a sufficiently high temperature that the thermal velocities of the nuclei are high enough to produce the required reactions, fusion brought about this way is called thermonuclear fusion. The provided energy has to be high enough to fully ionize the fuel and it is around 10 keV ($\sim 100\text{million}^\circ\text{C}$), and plasma is obtained, in this state the electrostatic charge of the nuclear ions is neutralized by the presence of an equal number of electrons.

As a D-T plasma is heated to thermonuclear conditions, the α particle heating provides an increasing fraction of the total heating. In adequate confinement conditions, a point is reached where the plasma temperature is maintained against the energy losses solely by α particle heating at this point the applied heating can be removed and the plasma temperature is sustained by internal heating (point called **ignition**). [37]

A certain amount of plasma heating, in tokamaks, is generated by the toroidal current flowing in the plasma itself, this plasma heating, at low temperatures is quite powerful. As the temperature of the plasma increases, the collision frequency and ignition resistivity fall. Around the ignition temperatures the

ohmic heating is much reduced, leading to requirement for additional heating, that is the reason behind the employment of NBI and radiofrequency heating.

The beams used for injection heating have to be composed of neutral particles because ions would be reflected by tokamak magnetic field. To produce a neutral beam, ions must first be produced and accelerated to the required energy. They are then neutralized by charge exchange in a gas target, and unwanted ions removed. In the plasma the neutral particles become charged again and as a result are confined by the magnetic field. They are then slowed by collisions with the plasma particles giving up their energy in process [37].

Given the high density expected for the DTT, to avoid a too peripheral power deposition the negative-ion-based NBI system is expected to work at energies $> 300keV$ [14].

NBI description Neutral Beam Injector (NBI) is already used as heating system in many existing magnetic confinement fusion devices. ITER is foreseen to have at least two NBI injectors and also DEMO will be provided with this technology. Beside the additional heating, NBI can also provide other functions like current drive and inducing plasma rotation [20].

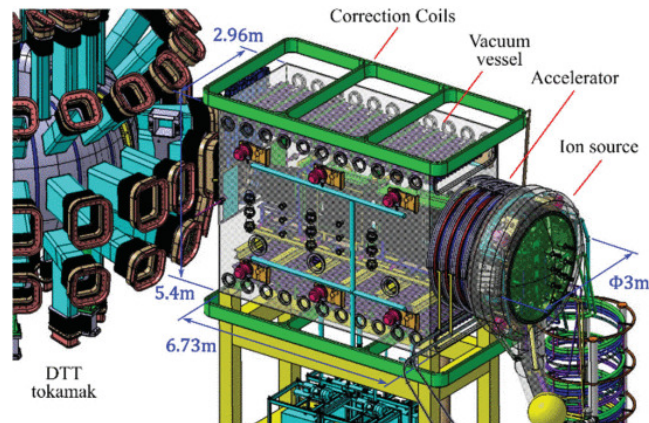


Figure 9: Neutral Beam Injector CAD representation, image taken from [35].

The neutral beam is obtained starting by either positive or negative ion beams, in fusion applications the second option is mostly chosen because it allows to produce high energy beams with a high neutral fraction[37]. Once the charged beam is obtained, it is accelerated and neutralized before the injection in the tokamak. The neutral beam, hence, is the result of different stages, which compose NBI:

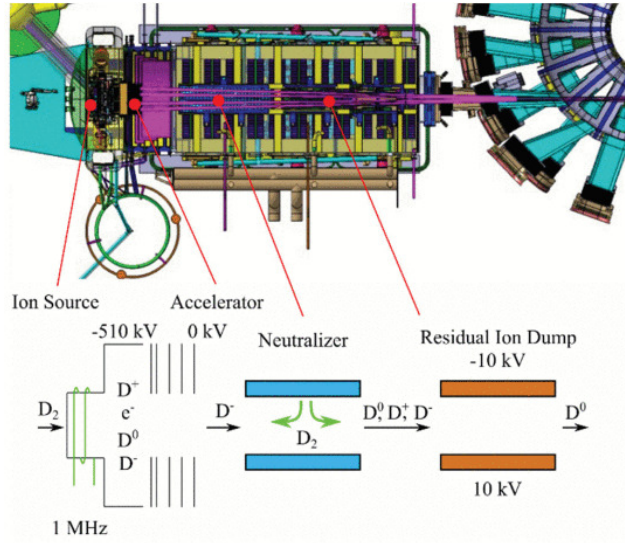
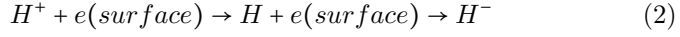
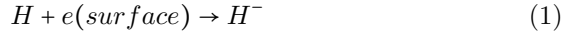
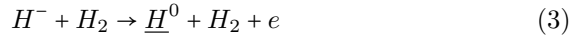


Figure 10: Neutral Beam Injector components, CAD and schematic representation, taken from [35]

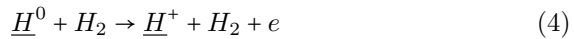
1. Ion source, in which plasma is generated and tanks to a catalyst (Caesium) negative ion extraction is enhanced [3], to obtain the D^- ions, the technology adopted is the surface production [19], this process is based on the transfer of electrons from the surface electrode to hydrogen atoms or ions approaching the wall [19]:



2. Accelerator, accelerate the D^- to an energy of 510 keV. This is made by means of a set of grids biased at different potentials[5].
3. Neutralizer. In this component, the negative beam is neutralized through collisional detachment, a process which happens thanks the neutralizer gas (deuterium), [26]:



but the process represented in section 3 is not the only one happening in the neutralizer, since the neutrals, by interacting with other neutralizer gas particles, experience also other processes, mainly ionization of fast neutrals:



(in section 3 and section 4 the underlined particles are the fast ones)

The process described by equation 4 is detrimental because it produces unwanted ions.

4. Residual Ion Dump (RID): the charged species in the beam are deflected by electric field onto the water-cooled panels of this component [17], which, according to [16], would be held the voltage around 12.5 kV dc, plus an alternate low-frequency component of about ± 2.5 kV, necessary to spread the power deposited by the deflected residual ions on the RID panels.
5. Calorimeter main purpose is to measure and analyse the power distribution of the neutral beam. It has to be able to absorb all the energy that is generated from the impact of the neutralized particles. In a closed position, the calorimeter has to intercept and remove the total beam power of 3.75 MW [24].

The neutralizer, Residual Ion Dump (RID) and calorimeter are called Beam Line Components (BLC).

2.3 DTT NBI design

The Neutralizer, as explained in section 2.2, is the BLC in which the neutralization process happens, it is made by 5 panels made of CuCrZr (figure 11), among which there is the neutralizer gas, these panels are connected together, in the upper and lower part, by horizontal flat elements.

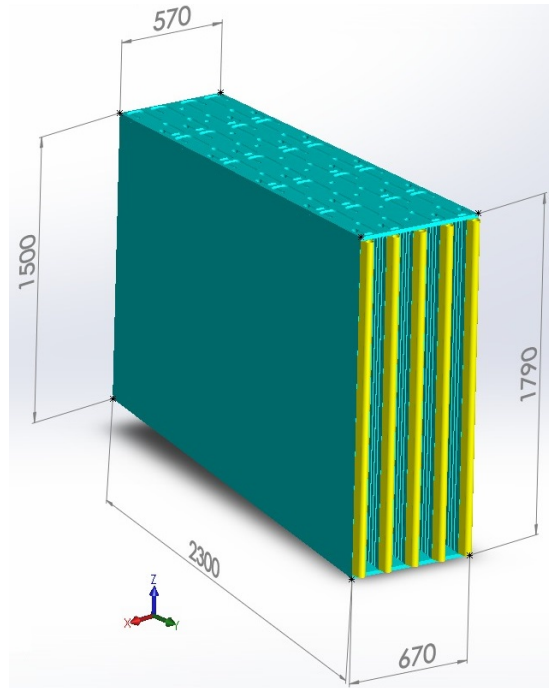


Figure 11: CAD visualization of the Neutralizer's panels (green), with their LEEs (yellow).

The magnetic confinement of the plasma is obtained by combining two magnetic fields, the toroidal and the poloidal one, generated by large set of super magnets, represented in figure 12. The toroidal magnetic field is generated by the toroidal field coils and confines the plasma in a toroidal shape, this alone is not enough, since the plasma tends to diffuse outward [37] The radial diffusion of plasma is controlled by the poloidal magnetic field, which is obtained thanks to the central solenoid in which flows a transient electrical current, this, due the transformer principle, induces an electrical current in plasma itself, current that will generate a magnetic field in the poloidal direction. In figure 13 there is a representation of the magnetic fields.

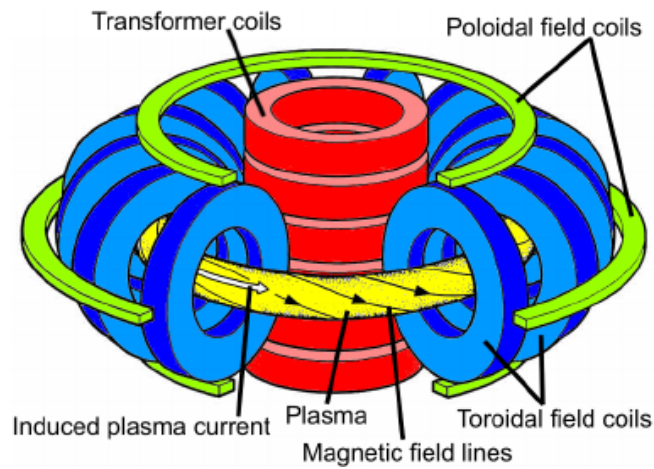


Figure 12: Magnet system of a tokamak [29].

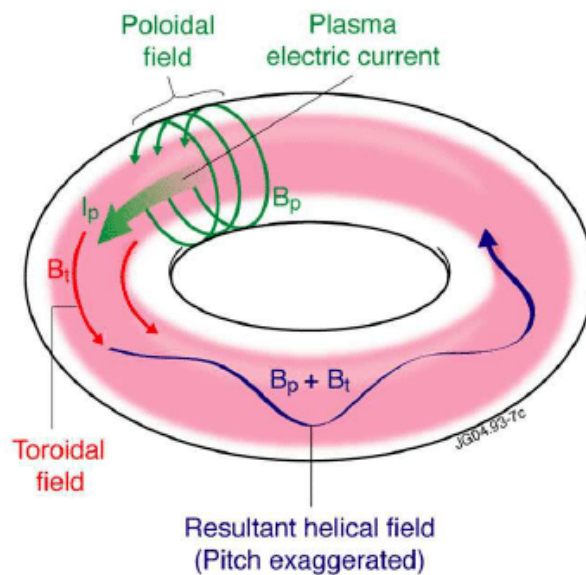


Figure 13: Representation of the poloidal and toroidal fields in the tokamak [25].

Although the toroidal field coils are discrete, part of the toroidal field escapes through the gaps between them, creating additional plasma losses, this field however decays quickly with increasing radial distance, thus it is not a problem for far enough devices. On the other hand, the problems arises regarding the poloidal field, since the magnetic dipole field around the tokamak expands freely, and the field decays slowly. This field is referred to as the "poloidal stray field". The charged beam in NBI, is susceptible to external electromagnetic fields, and since, as just explained, the poloidal field exapands way over the plasma domain, a magnetic shield is foreseen also in neutralizer, so its 5 CuCrZr panels,

cited above, are enclosed in the Stray Field Shielding System (SFSS), a steel component represented in figure 14, whose thickness is around 3 cm and it is foreseen to be built in SS400 steel[?]. The presence of the SFSS could lead to an increment of gas density, which can lead to stripping in the accelerator (the particles neutralize before their acceleration [2]), therefore some apertures (100 mm diameter) in the zone between the accelerator and the neutralizer will promote the gas flow and avoid this issue [34].

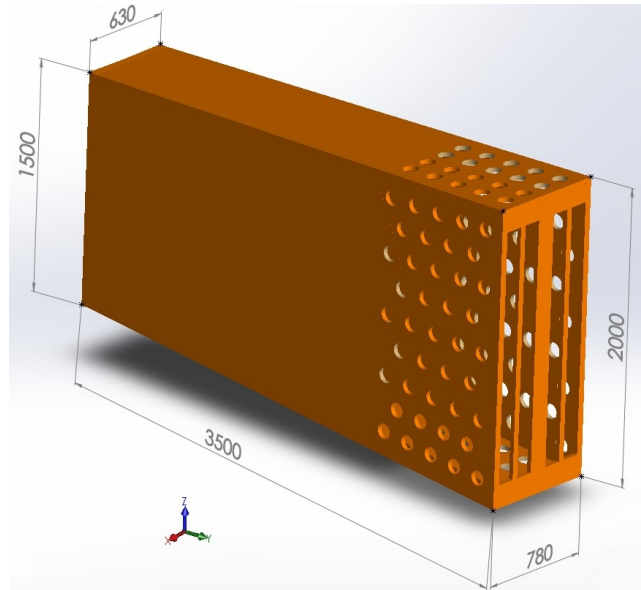


Figure 14: CAD visualization of the Neutralizer's SFSS

The flux exiting the accelerator hits the Neutralizer components resulting in heat deposition, therefore active cooling through water flowing inside the panels and the SFSS is foreseen.

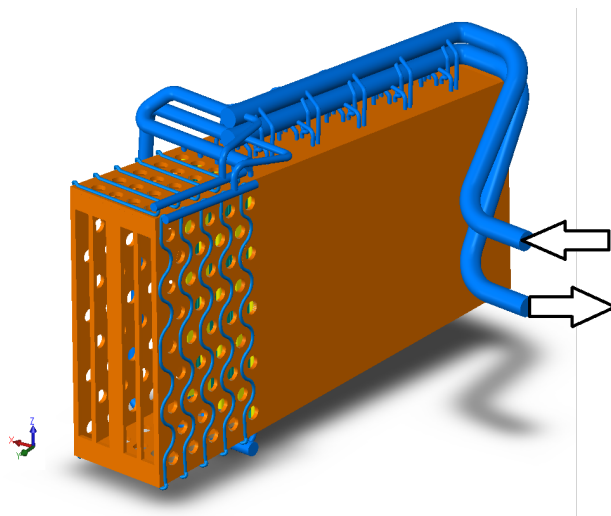


Figure 15: CAD visualization of the Neutralizer and its cooling system. The arrows point the flow direction.

One of the sides of the panels faces the beam: the Leading Edge Element (LEE), represented in figure 11, to avoid an extreme heat deposition over there, the heat exchange is enhanced in their cooling channels, as it will be described in detail in 3.2.1.

During the collaboration with RFX team, some geometrical details were changed, so there will be a reference to a design 1, design 2 and design 3.

2.4 Aim of the work and methodology

Thermofluid dynamic evaluation In section 3 are reported the thermofluid dynamic evaluations. Since the neutralizer is still in the design phase, during this study, made by RFX Team, as anticipated, made some changes of the CAD [4]. In the design 1, the panels are flat, in september 2023, the CAD was updated in design 2 (the updated version) the lateral surfaces of the panels have a particular shape CSS, described in 3.4.1, which enhance the neutralizer capability of keeping the gas between the panels, obtained the design 2 simulation results a further update of the design was implemented and in design 3 an additional coolant pipe is added. The complex 3D geometry of the component, the thermofluid-dynamic simulations were performed not always considering the whole domain:

1. in design 1, the whole SFSS is excluded by the simulation since it does not experience any heat load, therefore its temperature distribution is not relevant.
2. in design 2, due to some geometrical problems in the definition of the geometry:
 - only the heat loaded parts of the SFSS were included in the preliminary simulation with fluid, panels, and LEEs; a separate simulation was performed including the whole SFSS with fluid.
 - once the CAD issues were fixed, a simulation considering the whole SFSS together with the fluid domain, panels and LEEs was carried out.
3. in design 3,

The simulations performed and the relative domains are summarized in table 1:

CAD vesion	Domain in thermo fluid symulation	
Design 1	Fluid domain LEEs Panels	
Design 2	Simulation A	Fluid domain LEEs Panels Heat loaded parts of SFSS
	Simulation B	Fluid domain SFSS
	Simulation C	Fluid domain LEEs Panels SFSS
Design 3	IN	

Table 1: Thermo fluid-dynamic simulations and their domains

Thermo-mechanic evaluations The components which experience an increment of temperature will experience a dilatation as well. The magnitude of the expansion magnitude is obtained thanks to thermal expansion coefficient: $\alpha[-/K]$.

Once the thermo-dynamic evaluations were performed, the temperature map obtained is then used, as shown in section 4, to evaluate the displacement and the stresses that are generated in the structure.

Numerical tool Star CCM+ is a numerical solver, this means that the differential equations governing the different phenomena, are discretized and solved in the each of the smaller elements in which the domain has been discretized, called cells. Therefore to use a numerical solver it is essential to firstly generate a volume mesh of the geometrical domain. To obtain a size of the cell which allows to have satisfying result without a too large computational cost, an evaluation has to be carried out, as explained in section 4.2. Mathematical models describing physics phenomena usually consist of a set of partial differential equations, which, together with constitutive equations (which link load and deformation), form a closed set of equations. The first step towards the solution for reducing the continuous set to a discrete set of algebraic equations is the discretization of the continuous space domain into the cells. Typical element shapes are triangles, quadrilaterals, tetrahedra, and hexahedra. In each element, the distribution of the dependent variables is constructed from the discrete values that the variables assume at specific locations, for example, at the element nodes or edges. Shape functions interpolate the discrete values to any other point in the element, providing the local (per-element) distribution of the dependent variables. Mapping operations between the local element domain and the global physical domain ensure that the variables are continuous across adjacent elements. All integrals are approximated with appropriate numerical techniques, leading to the final set of discrete algebraic equations [28].

3 Thermal-fluid dynamics evaluations

In this section the results obtained by simulating in Star CCM+ the Neutralizer's components together with the cooling fluid are presented. The fluid dynamic simulation focuses on:

- The evaluation of temperature in both solid and fluid domain
- The evaluation of the pressure in the fluid domain, checking that the pressure drop remains below 6 bar

Boundary conditions As just anticipated at the end of section 2.4 simulations are made on three versions of the design. All of the three design versions have common boundary conditions:

- Inlet mass flow rate : 40kg/s
- Outlet pressure (gauge): 0Pa

The three have not only geometrical differences but also different thermal boundary conditions:

Design 1 Here the heat loads are imposed on the LEE and on the panels' sides. So, the whole SFSS has been excluded by the simulation since the absence of heat load over it, and it is not fundamental for the results.

Design 2 In the second one the heat loads are imposed on the LEEs, on the panels' sides and on two portions of the SFSS, due CAD (Computer Aided Design) geometrical problems:

Firstly, of the SFSS only heat loaded parts were included in the simulation with fluid, Panels and LEEs, and then in a separate simulation just the whole SFSS with fluid were taken in consideration.

Secondly, once the CAD issues were fixed, a simulation which considered also the whole SFSS was carried out. .

Design 3 The heat load and the domain is the same of the second one.

3.1 Introduction

3.1.1 physic continua

Physics continua are used in Star CCM+ to define physics of a certain substance, they are described through the chosen models. During the thermo-dynamic simulations three phisic continua have to be defined: the one referred to the CuCrZr, the one to steel and the one to water.

Water physics continuum

Space : the aim of this work is to have an idea on how the system behaves in its totality, so the definition of space the chosen model is three dimensional.

Time : stationary.

Material : liquid, in the pipes there is water.

Flow[28] : the segregated flow solver, solves the integral conservation equation of mass and momentum sequentially. In the segregated solver the mass conservation constraint on the velocity field is fulfilled by solving a pressure-correction equation.

Equation of state[28] : the choosen equation of state for the water is IAPWS-IF97. The models of IAPWS-IF97 are employed in simulations of liquid water or gaseous steam and include calculations of thermal-fluid dynamics properties.

The IAPWS-IF97 provides fundamental polynomial equations for the specific Gibbs free energy, $g(p, T)$ [8] Using appropriate combinations of the dimensionless Gibbs free energy and its derivatives it is possible, then, to retrieve specific volume, internal energy, entropy, enthalpy, heat capacity, and speed of sound. The IAPWS-IF97 models in Simcenter STAR-CCM+ are only valid within certain ranges of temperature and pressure, shown in figure 16

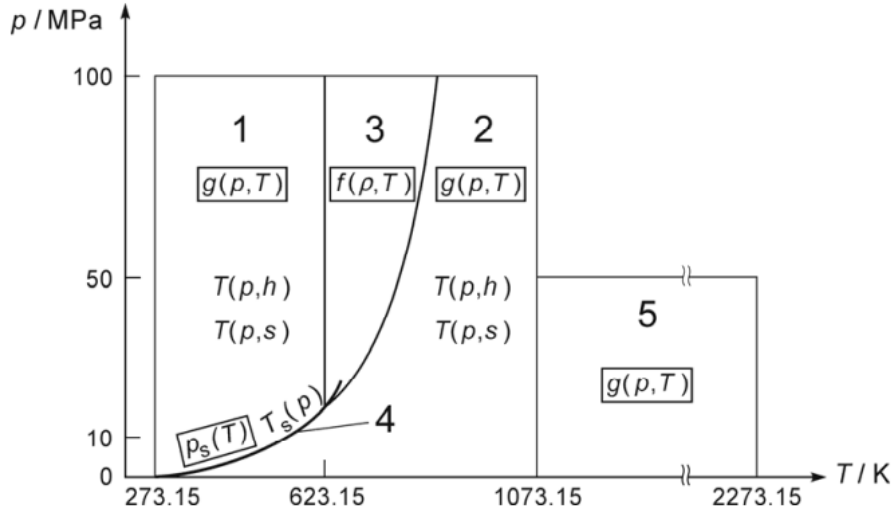


Figure 16: Regions and equations of IAPWS-IF97 [11]

The following table lists the components of the region diagram and how they work with IAPWS-IF97 models in Simcenter STAR-CCM+.

Components	Ranges of Validity		STAR-CCM+ Models
Region 1 (liquid)	$0^{\circ}\text{C} \leq T \leq 350^{\circ}\text{C}$ $273.15\text{K} \leq T \leq 623.15\text{K}$	$p \leq 1000\text{bar}$ $p \leq 100\text{MPa}$	IAPWS-IF97 (Water)
Region 2 (steam)	$0^{\circ}\text{C} \leq T \leq 800^{\circ}\text{C}$ $273.15\text{K} \leq T \leq 1073.15\text{K}$	$p \leq 1000\text{bar}$ $p \leq 100\text{MPa}$	IAPWS-IF97 (Steam)
Region 3 (saturation)	This phase region is not supported in Simcenter STAR-CCM+.		
Boundary 4	This boundary lies between liquid and saturation on one side, and steam on the other.		
Region 5 (steam)	$800^{\circ}\text{C} \leq T \leq 2000^{\circ}\text{C}$ $1073.15\text{K} \leq T \leq 2273.15\text{K}$	$p \leq 500\text{bar}$ $p \leq 50\text{MPa}$	IAPWS-IF97 (Steam)

Table 2: IAPWS-IF97 Regions of validity

During the simulations presented in this work, water conditions will be always within the limits of Region 1, highlighted in red in table2.

Energy [28]: Segregated fluid temperature model is chosen, this means that temperature is considered as the solved variable of the energy equation and segregated solver unlike coupled one, solves the conservation equations for continuity and momentum separately, this, even if it takes longer time to get the solution, usually requires less memory and it is more stable.

Enthalpy is then computed from temperature according to the equation of state.

viscous regime To handle the turbulent behaviour of the fluid, averaged quantities of the turbulent flows and approximation of the impact are used.

Turbulence models provide different approaches for modeling these structures. Shear stresses in fluid are found through Reynolds-Averaged Navier-Stokes (RANS) equation.

RANS turbulence models provide closure relations for the Reynolds-Averaged Navier-Stokes equations, that govern the transport of the mean flow quantities. For the present work the k-epsilon turbulence model is chosen. The K-Epsilon turbulence model is a two-equation model that solves transport equations for the turbulent kinetic energy and the turbulent dissipation rate in order to determine the turbulent eddy viscosity.

CuCrZr CuCrZr alloy has an excellent thermal conductivity, strength at high temperatures, ductility, toughness, machinability, water-tightness, and only moderate activation that is why it is also one of the most favoured heat sink material used for the Plasma-Facing Component (PFC) of major fusion devices [39].

The models selected to describe this material are the following:

Space: Three dimensional

Material: Solid. In Star CCM+, CuCrZr alloy is not present in the database of materials, thus, to obtain the proper material behaviour, were used the following properties:

- Specific heat:

$$c_p[\text{J/kg}\cdot\text{K}] = 6.32\text{E-}06 \cdot T^2 + 9.49\text{E-}02 \cdot T + 3.88\text{E+}02$$

With T expressed in °C, the relation is valid in the range: $20 < T < 700^\circ\text{C}$

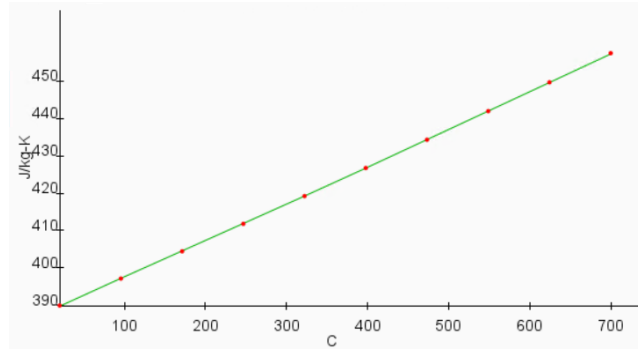


Figure 17: Plot of c_p , function of T.

- Thermal conductivity:

$$\lambda[\text{W/m}\cdot\text{K}] = 2.11\text{E-}07 \cdot T^3 - 2.83\text{E-}04 \cdot T^2 + 1.38\text{E-}01 \cdot T + 3.23\text{E+}02$$

With T expressed in °C, the relation is valid in the range: $20 \leq T \leq 700^\circ\text{C}$

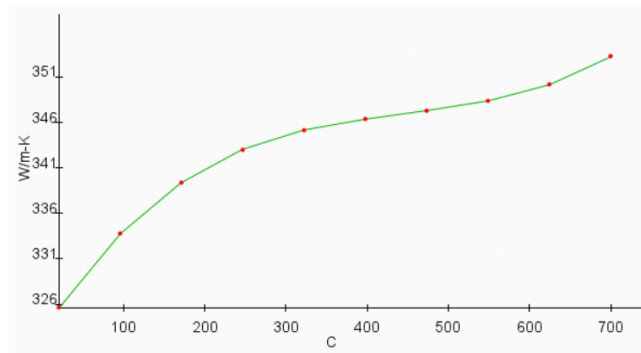


Figure 18: Plot of λ , function of T.

- Density:
 $\rho[\text{kg}/\text{m}^3]=8940$
Time: Steady
Equation of state: Constant density
Segregated solid energy

Steel The selected material for SFSS is the SS400, low carbon steel.

Space: Three dimensional

Material: Solid. To obtain the proper material behaviour, was used the following expression of the thermal conductivity [31]:

$$\lambda[\text{J}/\text{kg}\cdot\text{K}] = 70 - 60 \cdot T / 1300$$

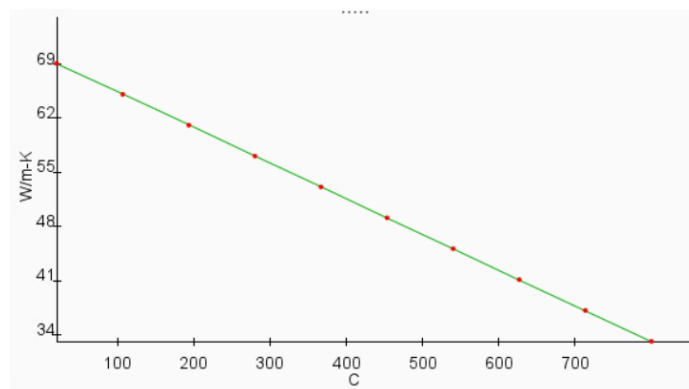


Figure 19: Plot of c_p , function of T.

- Time:** Steady
Equation of state: Constant density
Segregated solid energy

3.2 Mesh characteristics

In this section the choice of the mesh parameters is presented. Due the geometrical complexity of the neutralizer, the grid independence analyses were performed on the most critical component, i.e. one LEE, whose geometry is shown in figure ??.

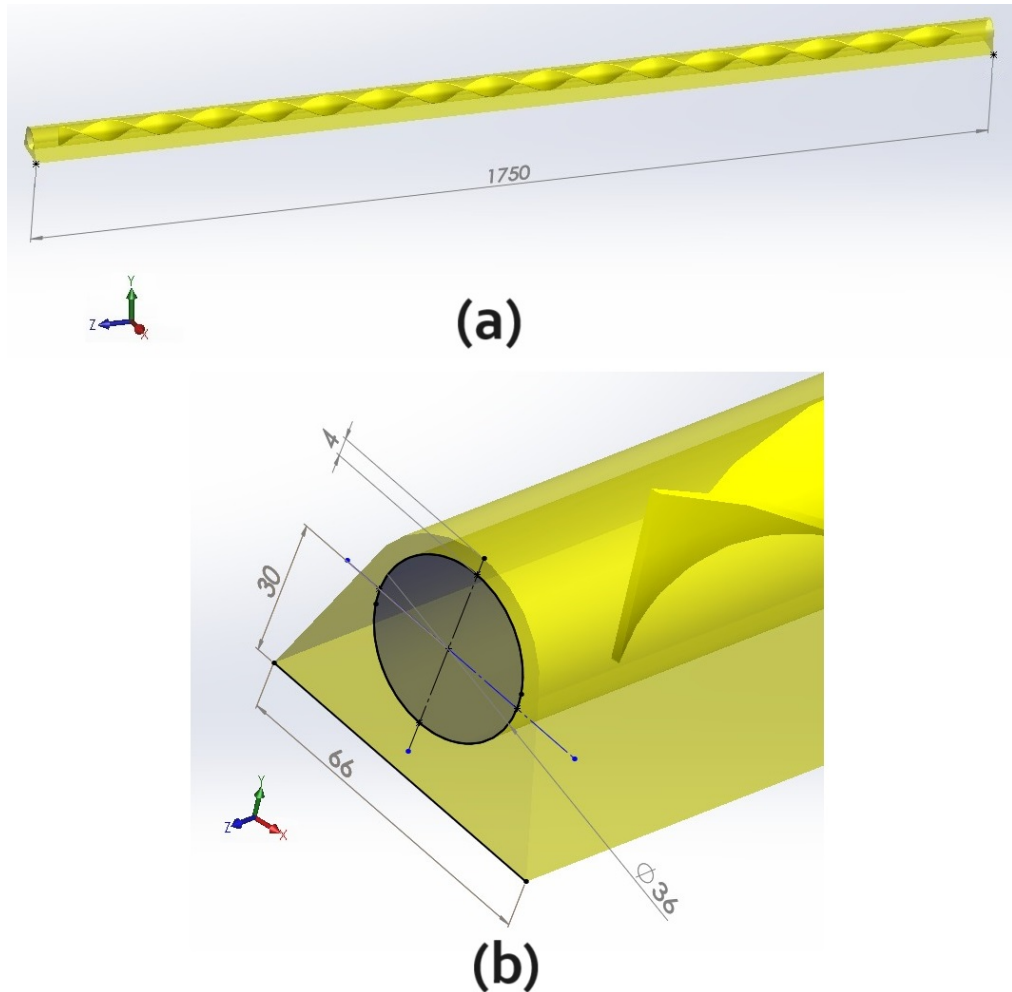


Figure 20: View of the CAD of a single LEE, used for the grid independence analysis, in (a) an overview, in (b) the profile.

3.2.1 Single LEE evaluation

The LEEs have the following dimensions:

The selected meshers are the following:

- Polyhedral mesher, this means that the cells will have a polyhedral shape like the one represented in

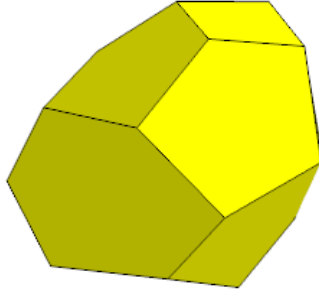


Figure 21: A 3D polyhedral cell.

- Prism layer mesher (prism layers are orthogonal prismatic cells next to wall surfaces or boundaries, necessary to improve the accuracy of the flow solution [28]; therefore, they are used only in the fluid domain)
- . The parameters which must be chosen are the following:
- Base size
 - Number of prism layers
 - Prism layer near wall thickness
 - Prism layer total thickness

Since the LEEs have to withstand a high heat load, a twisted tape positioned inside the pipe (Figure 3) enhances the coolant turbulence to increase the heat exchange.

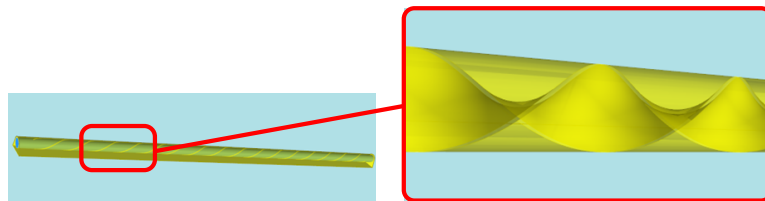


Figure 22: LEE structure, with a zoom on the swirl tape inserted in the cooling channel to enhance the turbulence.

The rest of the piping of the neutralizer (in the panels and SFSS) presents a common cylindrical shape (without any turbulence promoter) and a lower heat load, thus the grid characteristics were chosen based on the analysis one of the LEEs, in particular the most loaded one which is the central one. All the LEEs are subjected to heat load due to both electrons and deuterium particles hitting their external surface, as evaluated by RFX team[30], which result in the heat load map shown in figure 23:

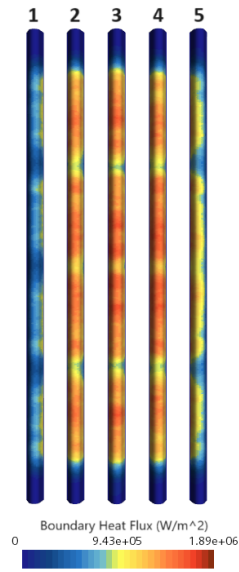


Figure 23: Heat load on LEE.

By making the integral of the heat flux over each of the LEE surfaces, it is possible to obtain the table 3, and to verify that the most loaded panel is the 3rd one.

	Heat load surface integral [MW]
LEE 1	0.5
LEE 2	1.1
LEE 3	1.2
LEE 4	1.1
LEE 5	0.7

Table 3: Result of the integral of heat load over each LEE loaded surface.

the central one, prescribing the heat load due the electron and deuterium fluxes; the resulting heat flux distribution is shown in Figure 24 [30].

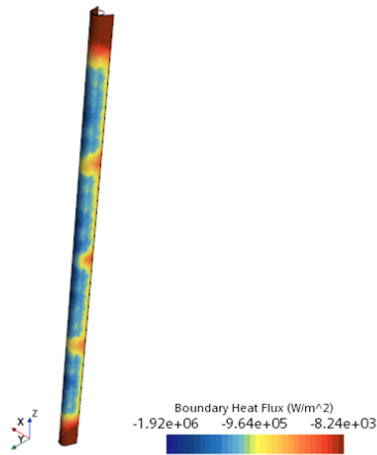


Figure 24: Boundary heat flux imposed on the LEE.

The massflowrate which cools each lee is assessed to be 2 kg/s, while the outlet pressure is considered to be 0Pa

Prism layer near wall thickness In the fluid domain, capture the wall phenomena induced in the flow by the viscous interaction with the pipes, a large number of closely spaced grid cells near the wall is needed at the boundary of the fluid domain [6], as represented in figure ??.

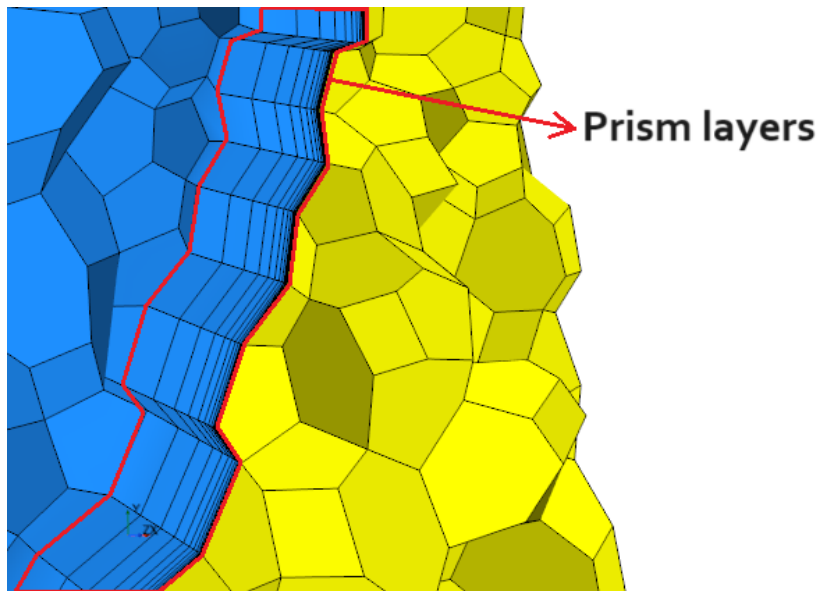


Figure 25: Representation of a prism layers.

Deciding the needed thickness of the prism layers near the wall is related to the thickness of boundary layer of the problem. .

The boundary layer (represented in figure 26), physically, is the fluid layer closer to the wall, which is affected by its presence. Due the viscosity, the velocity of the fluid approaches 0 as it gets closer to the wall, the viscous sub layer, red colored in figure 26 is the closest to the wall where the viscous phenomena are greater than the inertial ones

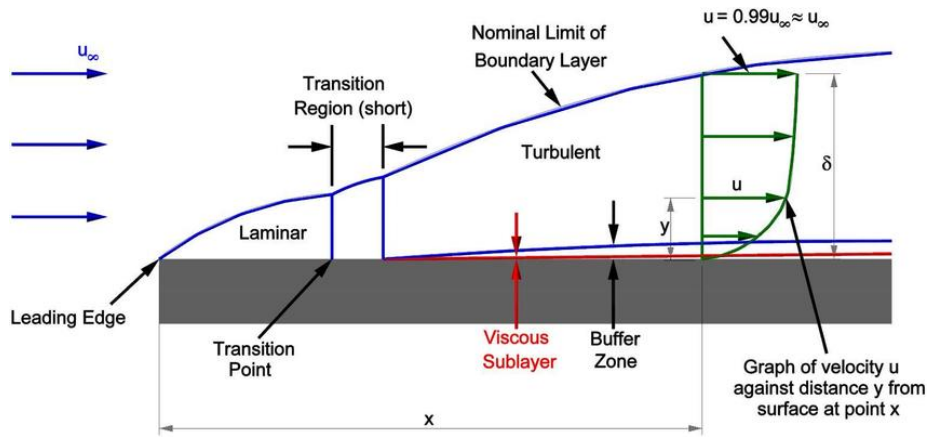


Figure 26: Visulaization of the boundary layer, from [33].

Considering the adimensional distance from the wall, y^+ and the adimensional velocity of the fluid, u^+ .

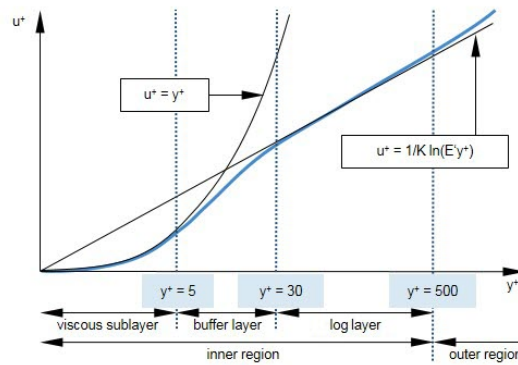


Figure 27: Representation of $u^+(y^+)$ [28]

It is necessary that, on the cells in contact with the wall, the y^+ value is around 1 to be sure that the viscous sublayer is modelled properly. The prism layer near wall thickness was changed until its range the rest of the mesh characteristics were kept fixed as reported in table 4

Mesh characteristic	Value
Base size	$2 \cdot 10^{-2}m$
Number of prism layers	7

Table 4: Gussed mesh characteristics values, which will be evaluated later.

The near wall prism layers thickness value was changed, until the non-dimensional distance from the wall y^+ value reached values around 1 all over the wall of the fluid domain, as reported in table 5.

Prism layer near wall thickness	y^+ range
No prism layers	$2.52 \leq y^+ \leq 259$
$5 \cdot 10^{-5}m$	$0.648 \leq y^+ \leq 12.2$
$\frac{5 \cdot 10^{-5}}{3}m$	$0.144 \leq y^+ \leq 4.6$
$\frac{5 \cdot 10^{-5}}{6}m$	$0.0938 \leq y^+ \leq 2.34$

Table 5: Prism layer near wall thickness and relative y^+ range.

Thus the prism layer near wall thickness was chosen to be $\frac{5 \cdot 10^{-5}}{6} \approx 8.3 \cdot 10^{-6}mm$, the result is shown in figure 28

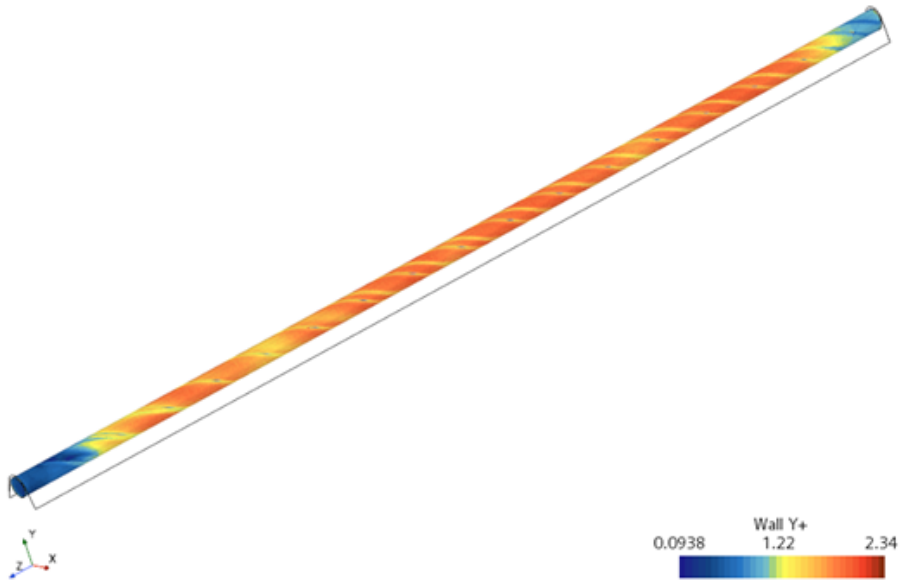


Figure 28: Color map of y^+ wall values in the single LEE

Base size This value specifies the reference length for some mesh controls which are:

- Target Surface Size, which specifies the face size that the mesher aims to achieve in absence of smaller mesh controls. This is settled as 100% of

Base Size

- Minimum Surface Size, which is the value below which the mesh edges below this size are removed, where feasible.

To determine this value, an assesment has been carried out, considering:

	Mesh characteristic	Value
Guessed	Number of prism layers	7
Evaluated previously	Prism layer near wall thickness	$8.3 \cdot 10^{-6} m$

Table 6: Mesh characteristics values used during Base Size evaluation.

A grid independence analysis has been used: the assessment consisted in changing the base size and observing a reference physical quantity result of the numerical evaluations, i.e. the maximum temperature both in solid and liquid. the following are the initial conditions:

- Inlet mass flow rate: 1.8 kg/s
- Outlet pressure 0 Pa

starting from the initial tentative value of $2 \cdot 10^{-2} m$, it was doubled and halved; according to the results reported in figure 29, the value of the base size was then considered to be $2 \cdot 10^{-2} m$.

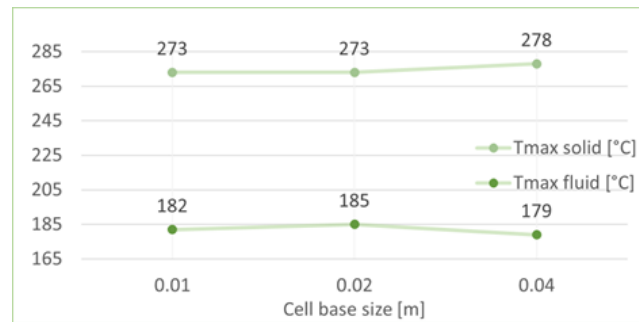


Figure 29: Maximum temperature in fluid and solid domains as a function of the cell base size.

By decreasing the base size, the number of cells increases, as shown in figure 30, and with it also the computational cost of the simulations, that's why the chosen base size is 0.02 m.

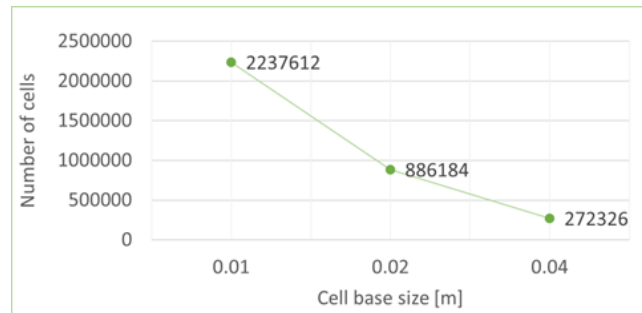


Figure 30: Number of cells as a function of the cell base size.

	Mesh characteristic	Value
Evaluated previously	Prism layer near wall thickness	$8.3 \cdot 10^{-6}m$
Evaluated previously	Base Size	$0.02m$

Number of prism layers Another grid Independence assessment is exploited to find the number of prism layer (described in 3.2.1), the compared values were: 7, 12 and 18, as in section 3.2.1 the numerical result considered is still maximum temperature in solid and fluid, the initial conditions for the simulation are as the ones used in section 3.2.1 too. In figure 31 the results are reported.

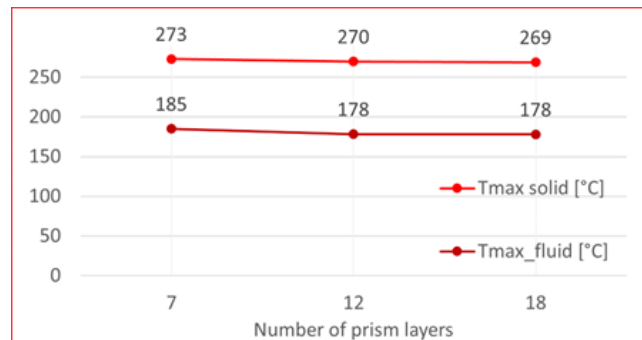


Figure 31: Maximum temperature in in fluid and solid domains as a function of number of prism layers,

While in section 32 there is the relation between the increase of the Number of the prism layers and the number of cells.

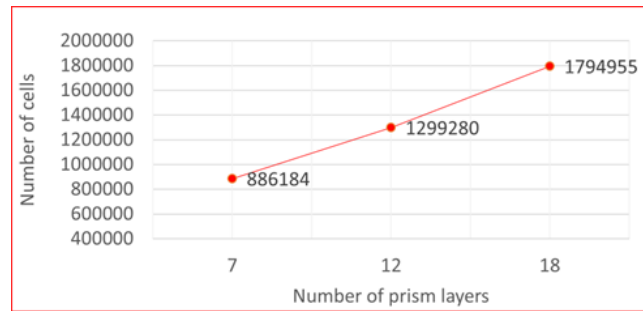


Figure 32: Number of Cells as a function of number of prism layers.

The value of 12 prism layers is then chosen since it is a good compromise between quality of numerical result and computational cost. Figure 33 shows a view of the resulting, grid independent mesh.

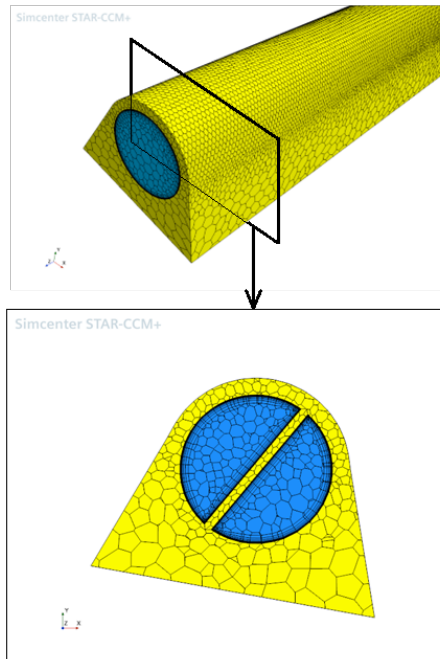


Figure 33: Grid independent mesh visualization.

Summarizing, the mesh parameters, which are adopted for all the following simulations, are reported in table 7:

Mesh characteristics	Value
Base size	$2 \cdot 10^{-2}m$
Number of prism layers	12
Prism layer near wall thickness	$8.3 \cdot 10^{-6}m$
Prism layer total thickness	$2mm$

Table 7: Mesh characteristics values used during simulations.

3.3 Neutralizer Design 1

3.3.1 Geometry and heat loads

Geometry In the first version of the Neutralizer's CAD (whose components are shown in figure 34) the panels have flat lateral surfaces, the internal diameter of the coolant pipes of the panels is $\phi = 30mm$, and there is the SFSS.

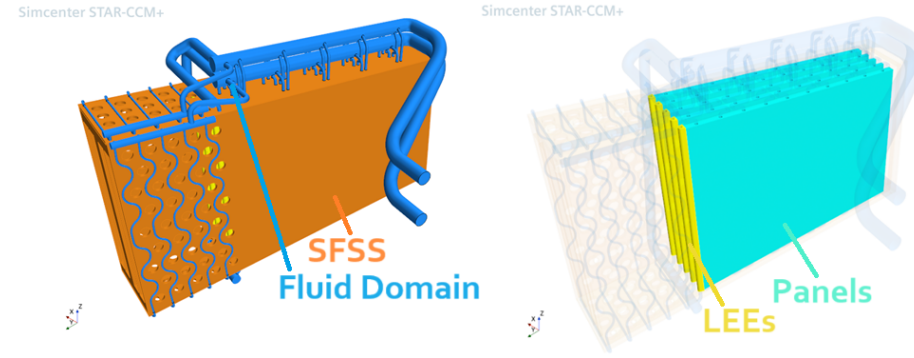


Figure 34: View of the neutralizer.

Heat loads The heat distribution is taken from [30]; the files, contain the value of heat load due to the electron and the deuterium flux, for each one of the LEE and panels sides, in some of the points of the loaded surfaces. These files, for each surface, are then interpolated to have a smoother heat load map, thus the final, combined heat load distribution is shown in figure 35.

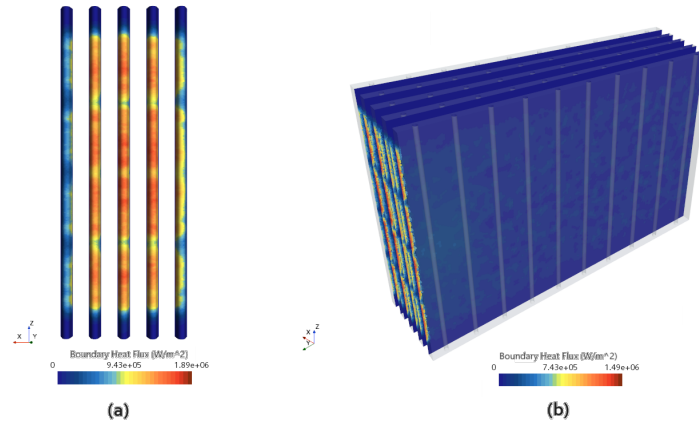


Figure 35: Resulting heat loads on (a) LEE and (b) panels.

3.3.2 Simulation and results

Since there's no heat load on the SFSS, in this phase of the simulation the component is not considered, thus reducing the computational cost. The following boundary conditions are adopted:

- Inlet mass flow rate: 40 kg/s
- Outlet pressure (gauge): 0 Pa

In Star-CCM+, then each component is associated with its physics continua as described in section 3.1.1 .

- Result of the hydraulic simulation are shown in figure 36:

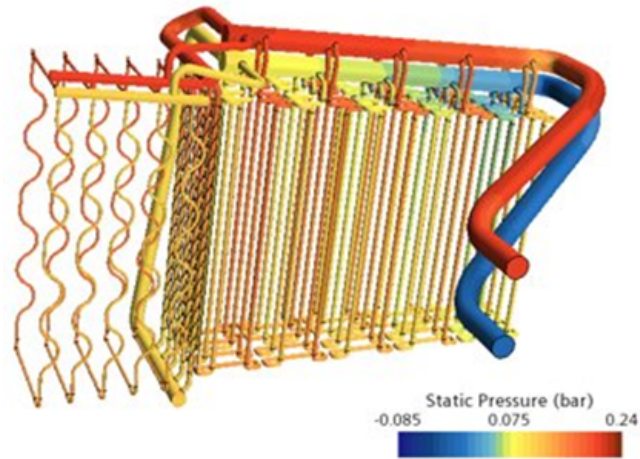


Figure 36: Pressure map in the fluid domain.

The pressure drop, between inlet and outlet is $\sim 0.26bar$, smaller than the limit

- Temperature distribution in both solid and fluid domain is shown in figure 37:

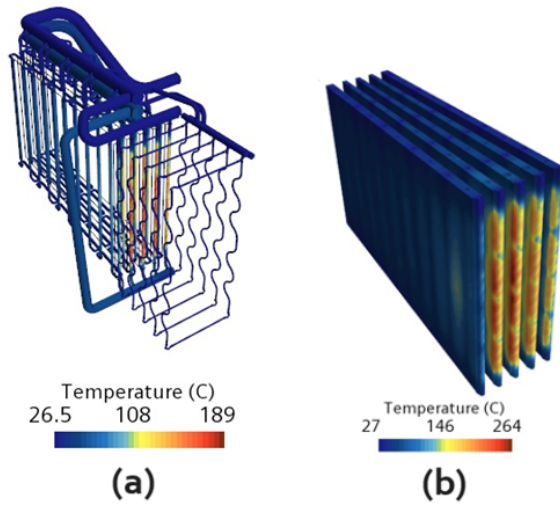


Figure 37: Temperature map on the surface of (a) fluid domain and (b) solid domain.

The maximum fluid temperature is 190 °C, well below the saturation temperature of 212 °C. The peak solid temperature is 265 °C. This temperature, even if in principle is well below the melting limit of the sold materials, should be decreased below 200 °C to prevent ageing or recrystallization.

- The repartition of the coolant mass flow rate is shown in figure 38

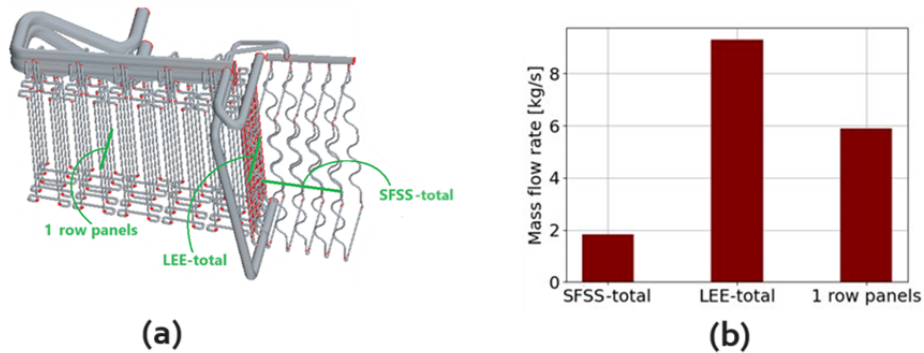


Figure 38: Sections of the fluid domain (a) in which massflowrate is evaluated and reported in (b).

3.4 Neutralizer Design 2

3.4.1 Geometry and heat loads

Geometry In September 2023, the geometry was updated [4]

- The lateral surface of the panels is not flat anymore, but it has a Cylindrical Sawtooth Structure (CSS) instead (shown in figure 39), to better contain the deuterium gas in the central part of panels.

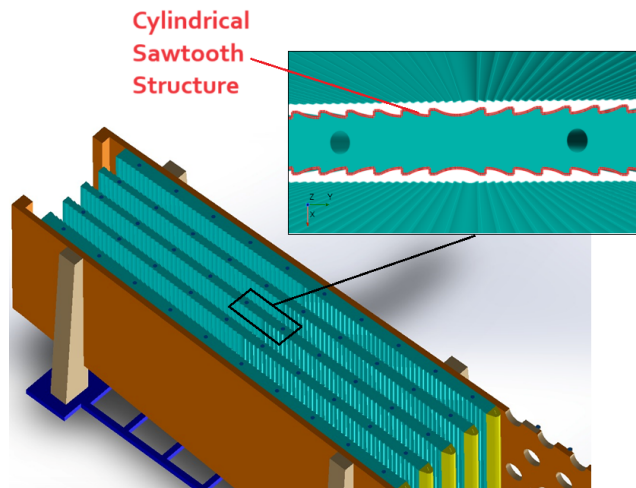


Figure 39: Horizontal section of the geometry, with a zoom on panel structure.

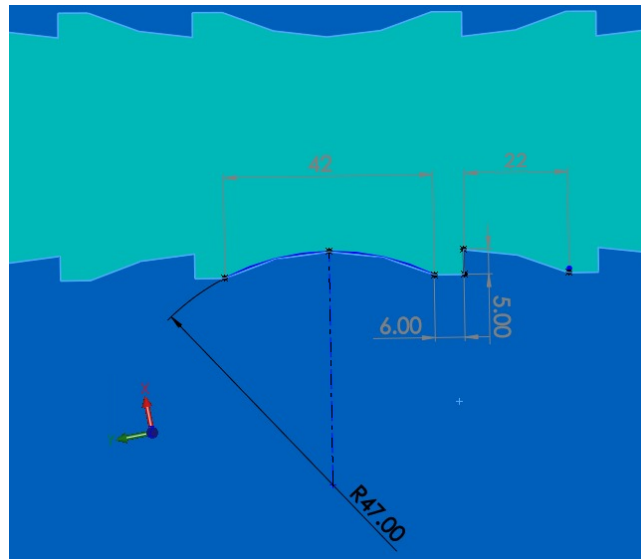


Figure 40: Dimensions of CSS

- The diameter of the coolant piping is decreased ($\phi = 20mm$) as shown in

figure 41

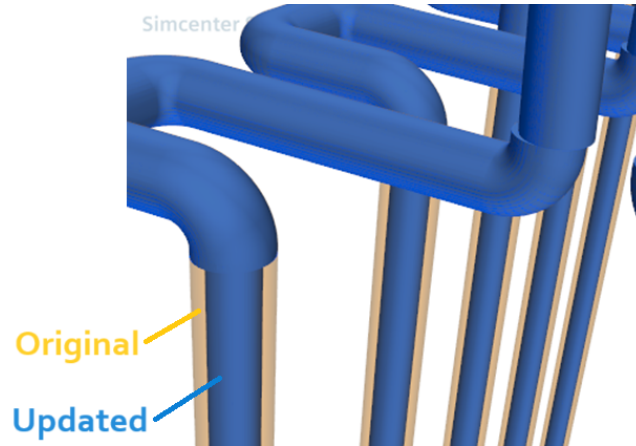


Figure 41: Comparison between original and updated design of the pipes cooling the panels.

Heat loads

- On the **LEEs** the heat load distribution is the same of that used in previous design (figure 35 (a)).
- On the **the panels** (see figure 42):
 - over the flat surfaces, the prescribed heat load is $0.14MW/m^2$
 - over the curved surfaces, the prescribed heat load is $0.036MW/m^2$

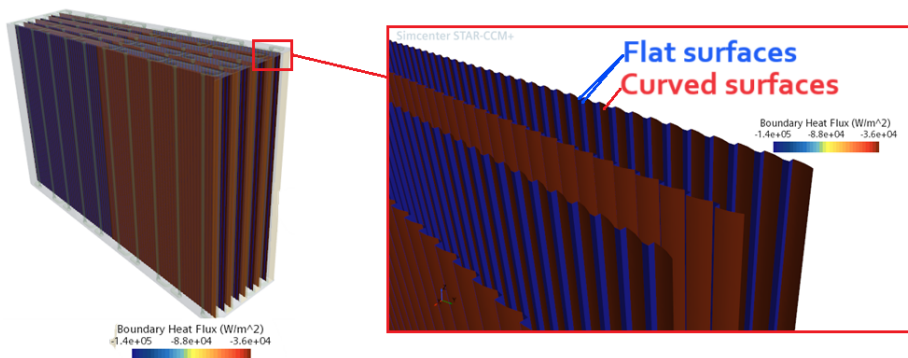


Figure 42: Heat load imposed on panels.

- On the **SFSS**, there is now a heat load on some portions of the surfaces, as reported in figure 43.

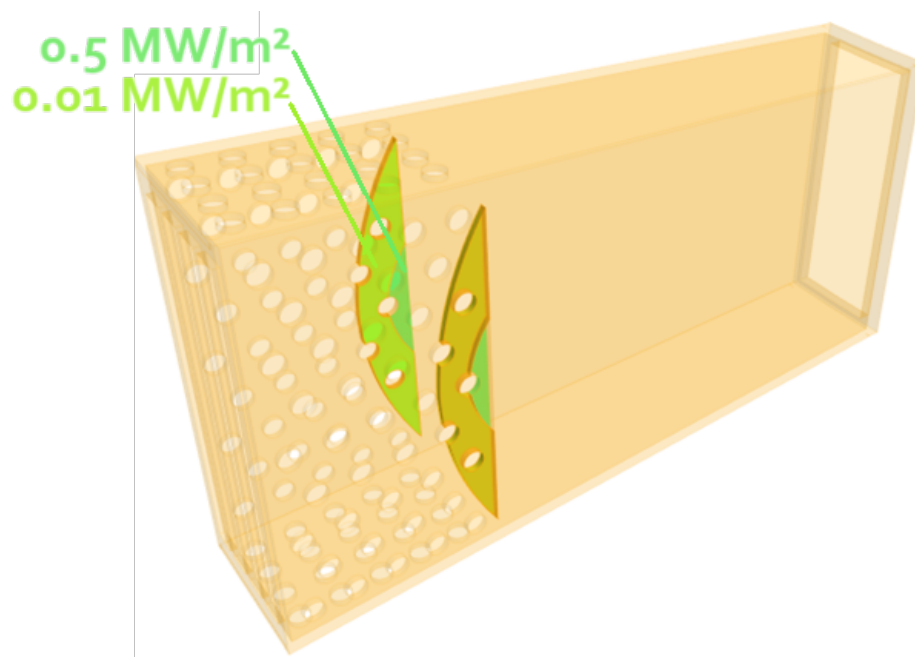


Figure 43: Heat load prescribed on SFSS.

3.4.2 Simulation and results

Since there were some problems while meshing the whole SFSS with the rest of the geometry, due to geometry intersections in the CAD, different simulations were carried out:

- A) Fluid domain + Panels + LEEs + parts of SFSS experiencing heat load
- B) Fluid domain + parts of SFSS experiencing heat load + the rest of SFSS
- C) Whole geometry (once the intersection problems in the CAD were fixed)

Simulation A In figure 44 there's a visualization of the domain modelled in the first simulation.

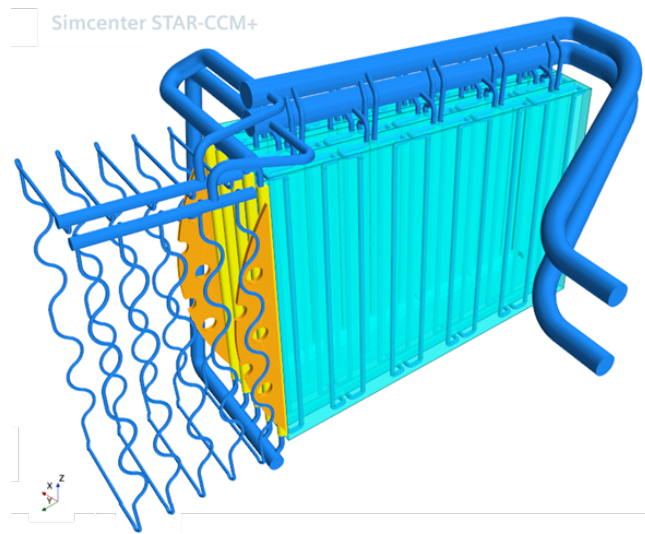


Figure 44: Solid and fluid domains considered in 1st simulation

Here the results are presented.

- The coolant pressure drop is increased by 50% (up to $\sim 0.4\text{bar}$) with respect to the previous design, see figure 36, but it is still well below the 6 bar constraint.

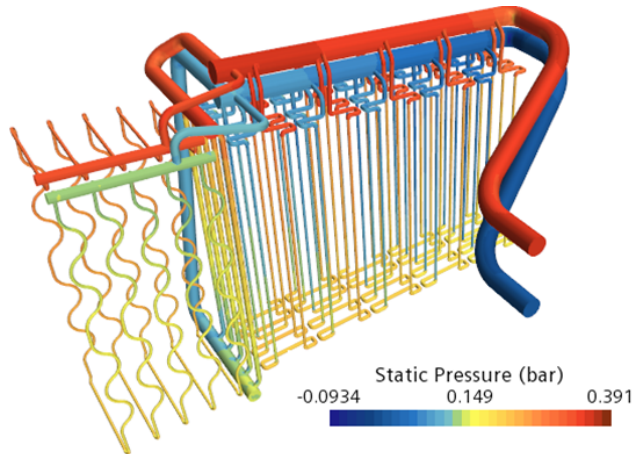


Figure 45: Pressure distribution in the fluid domain.

- The temperature maps both in solid and fluid domains are reported in 46

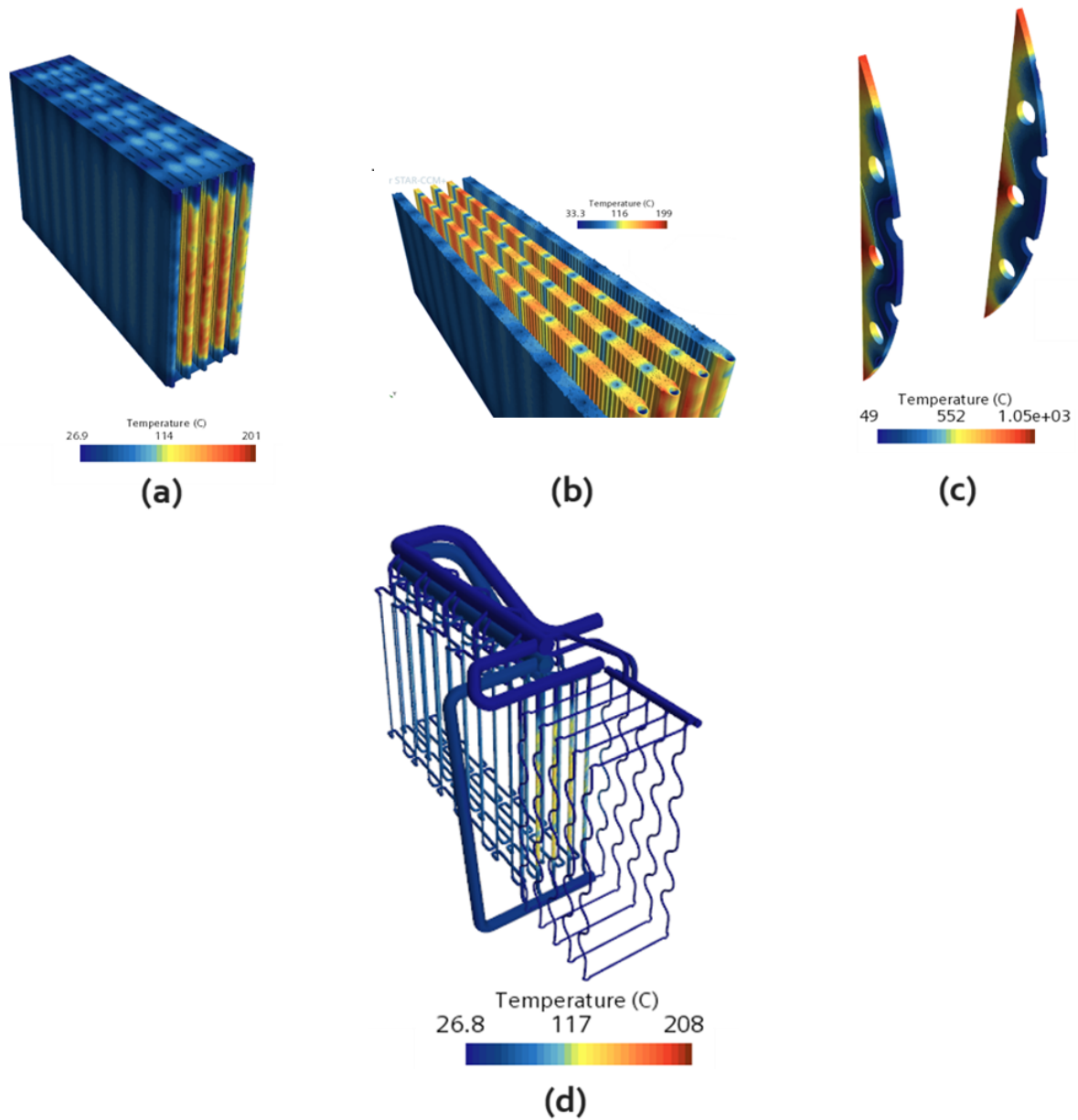


Figure 46: Temperature map (a) in panels and LEEs, (b) an horizontal section of panels and LEEs (c) heat loaded portions of SFSS and (d) fluid domain.

As we can observe from the temperature maps (figure 46), while in the CuCrZr and in the coolant the temperature remains within the limits, in the steel domain, i.e. the parts of SFSS experiencing heat loads, the temperature raises over acceptable values. This requires additional simulations to investigate if this is due to the limited SFSS part included in

the domain or it could be a real problem of the design.

- Mass Flow Rate: as seen in Figure 47., the mass flow rate is evaluated in different sections on the new fluid domain as it has been done in figure 38 with the previous design. Since the diameter of the pipes cooling the panels decreased by 10 mm, the decreased coolant mass flow rate in the panels and the increment in the LEEs were both expected.

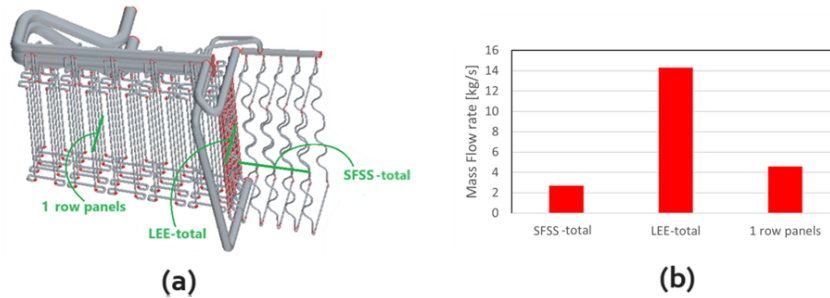


Figure 47: Sections of the fluid domain (a) in which massflowrate is evaluated and reported in (b), in the updated geometry.

Simulation B In this case only the SFSS with the entire fluid domain was modeled to assess if the temperature in the heated parts of SFSS decreases due the conduction towards the rest of the component. Figure 48 reports the domains of the 2nd simulation.

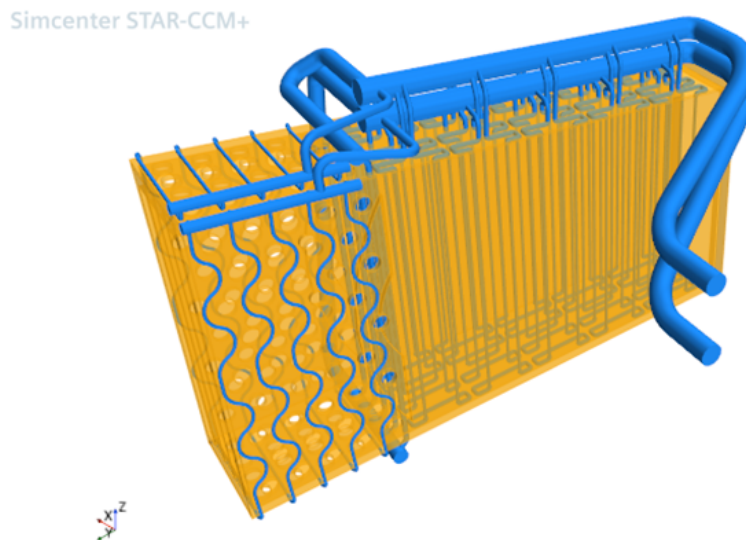


Figure 48: Solid and fluid domains in 2nd simulation.

- In figure 49 the temperature map in the steel domain is presented.

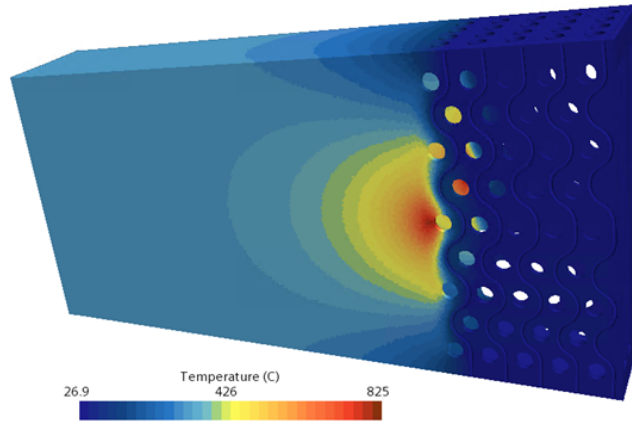


Figure 49: Temperature map in SFSS.

Comparing figure 49 and figure 46(c), it is possible to observe that the presence of the rest of the SFSS helps to decrease the temperature in the steel domain, even if it remains too high. However, it is expected that the panels and LEEs could further contribute to decrease it.

Simulation C The domain considered during this simulation, includes all the components of the original CAD (figure 51), the geometrical problems, arose previously, were fixed by simplifying the geometry of the panels: the 5 panels don't have the horizontal connection on top and base, highlighted in cyan in figure

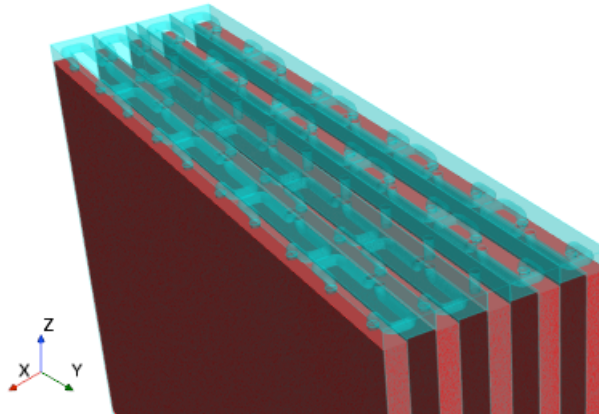


Figure 50: Visualizalization of the horizontal connection between panels in the top part.

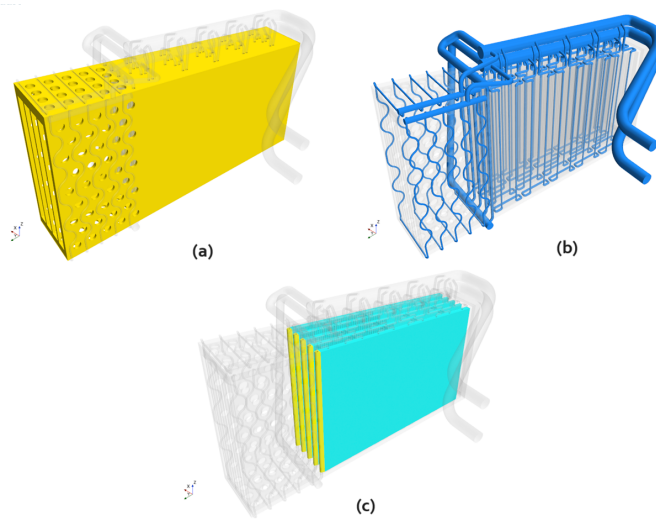


Figure 51: Solid and fluid domains in 3rd simulation: (a) the SFSS, the fluid domain (b), panels and LEE (c)

after the simulation, the results obtained are the following:

- Pressure map in fluid domain is shown in figure 52:

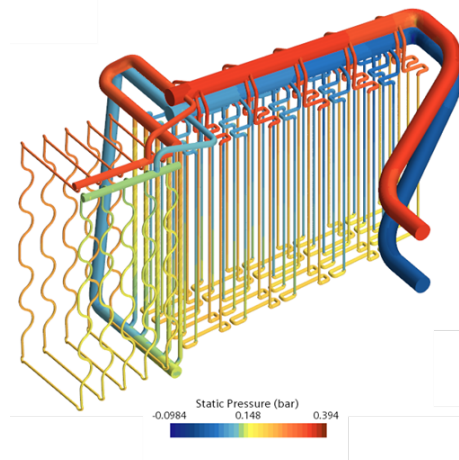


Figure 52: Pressure field in the fluid domain.

- The temperature in SFSS is shown in figure 53:

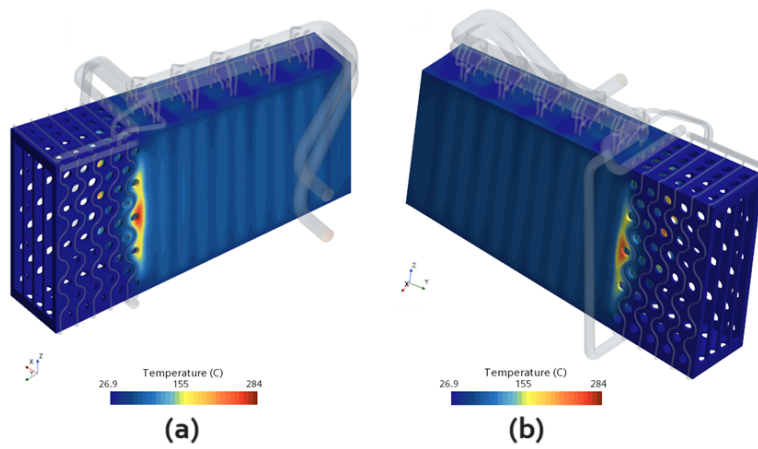


Figure 53: Temperature map on the SFSS: showing its vertical lateral surface in **(a)** the one with the normal oriented towards negative x and in **(b)** the one with normal oriented towards positive x.

In the fluid domain, the temperature map is the following:

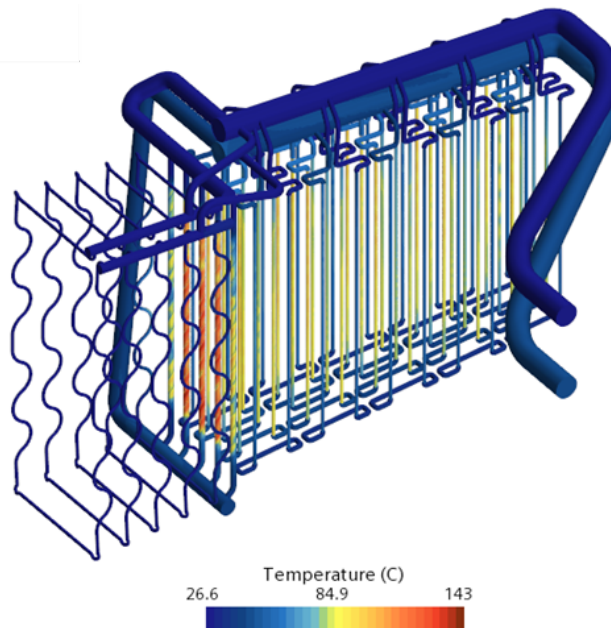


Figure 54: Temperature map on the surface of the fluid domain.

Finally in figure 55 is reported the temperature map of the LEE and panles:

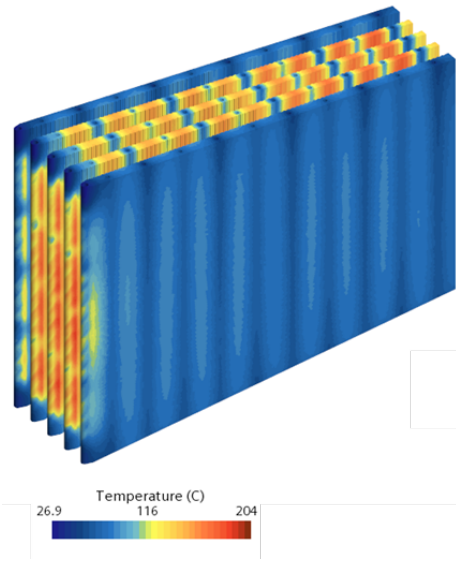


Figure 55: Temperature map on the surface of LEEs and panels.

3.4.3 Summary of Design 2 thermal-fluid dynamics results

Once the results of thermal-fluid dynamics evaluations made on the design 2, were presented it could be interesting to summarize and compare the different results to stress similarities and difference in order to assess in which way the geometrical simplifications adopted influenced the results.

SFSS Looking at the maximum temperature in SFSS domain for each one of the 2nd update design simulations, it is possible to report all the values on a graph, reported in figure 56, which gives an hint on how it is important to take in consideration all the parts present in the CAD: in 3rd simulation, the temperature on SFSS has largely decreased if compared with the 2nd and 1st simulation, due to the possibility to transfer part of the heat deposited on the loaded parts of SFSS, by conduction to the adjacent part of the component and to the panels.

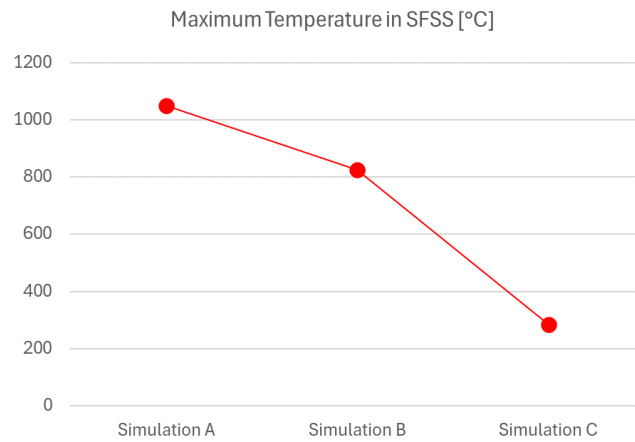


Figure 56: Comparison among the maximum temperatures in steel domain, evaluated in the different thermo dynamic simulations of the 1st upgrade design.

As previously mentioned, this component is made of SS400 steel [31], in particular ,

Panels and LEEs These components were taken in consideration in the 1st and 3rd simulation, it is possible to plot their the maximum temperature, as reported in figure 57:

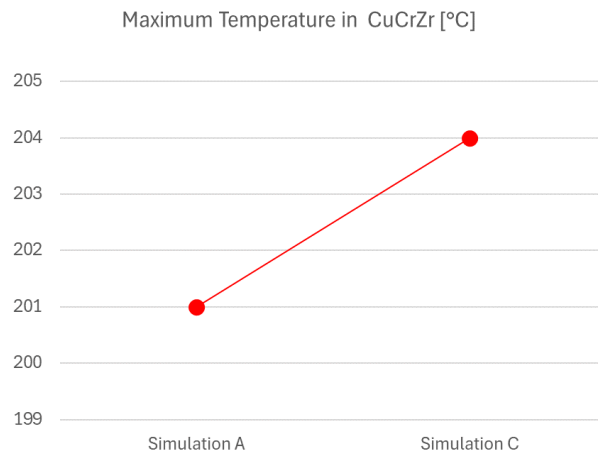


Figure 57: Comparison among the maximum temperatures in CuCrZr domain, evaluated in the different thermo dynamic simulations of the 1st upgrade design.

As it is possible to notice from the figure above, the first and last simulation have different computed maximum temperature of Panels and LEEs, the increment

probably is due the presence of contact with SFSS which is hot and transfers heat to the CuCrZr components.

Water Still comparing the A and C simulations, water maximum temperature decreases

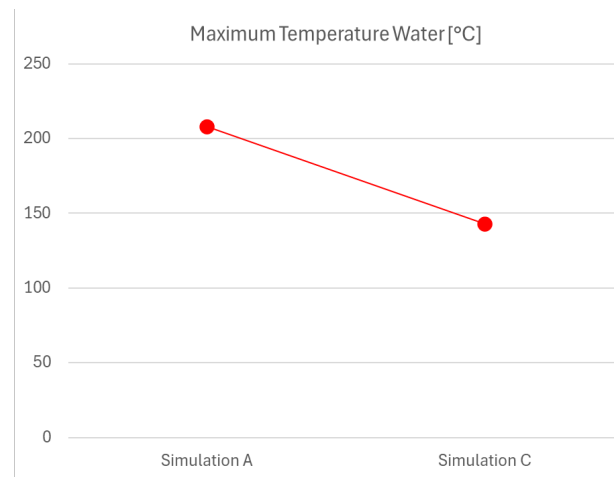


Figure 58

3.5 Neutralizer Design 3

In February 2024, the RFX team, after the visualization of results in reported in the thermo-dynamic evaluations of the 1st update design, added a coolant pipe to the cooling system of the SFSS, as seen in figure 59:

Simcenter STAR-CCM+

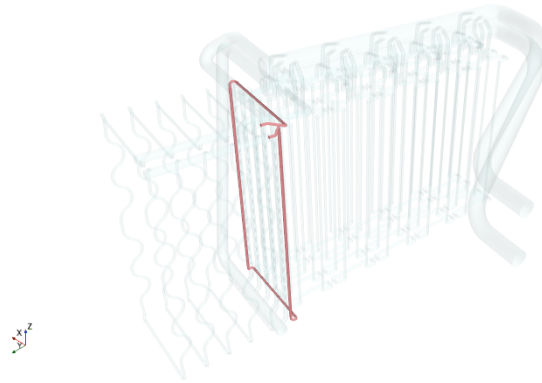


Figure 59: Additional coolant pipe highlighted in red.

3.5.1 Geometry and heat loads

The overall neutralizer geometry is still the same of design 2 with the difference of the additional the coolant pipe. Even the heat loads are the same of design 2.

4 Thermomechanic evaluations

thermal expansion coefficient melting temperature Since the body experiences an increment of temperature, it is interesting also to assess which is the following deformation and stresses distribution. This evaluation is particularly important in this case because the displacement must not to interfere with the beam. All the solid parts were interested by this type of evaluation and for sake of simplicity were studied separately. To assess the displacement and the stress generated in the structure under the thermal load, it is necessary to use a stress solver which bases on a finite element method, The Finite Element method is a powerful tool for finding approximate solutions to continuous problems. The methodology is similar to other numerical techniques that approximate continuous partial differential equations with discrete algebraic equations. Simcenter STAR-CCM+ currently uses the Finite Element method in Solid Mechanics.

4.1 Introduction

4.1.1 Physics continua

The components whose deformation and stress map are assessed in the present chapter, are the panels and the SFSS, as already explained previously (in section 2.3) the first one is a part made of CuCrZr and the other STEEL. To perform the thermo-mechanic evaluations is necessary define new physics continua, still referred to the same materials in section 3.1.1, except, obviously, the water one.

CuCrZr The models chosen are the following:

Space: three dimensional

Time: steady

Material: solid. To model correctly the behaviour of CuCrZr, is considered the temperature dependence of the thermal expansion coefficient, thus, by starting from table 8 :

T [K]	α [-/K]
293.15	1.67E-05
323.15	1.70E-05
373.15	1.73E-05
423.15	1.75E-05
473.15	1.77E-05
523.15	1.78E-05
573.15	1.80E-05
673.15	1.81E-05
723.15	1.82E-05
773.15	1.84E-05
823.15	1.85E-05
873.15	1.86E-05

Table 8: Puntual values of α as function of the temperature.

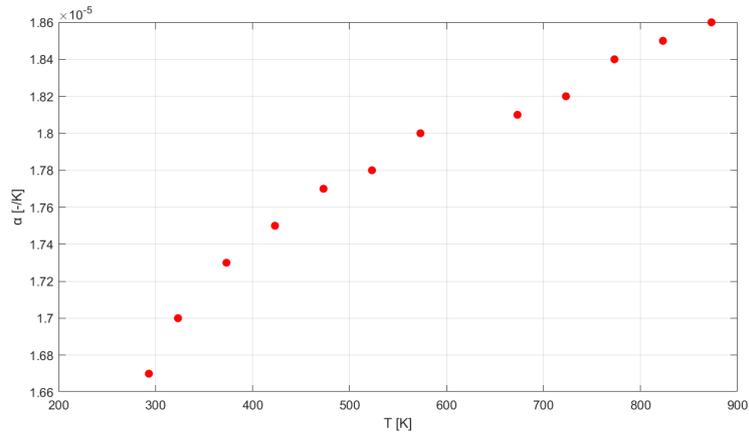


Figure 60: Visualization of (T, α) points on chart.

In Star CCM+ there's the possibility of interpolate points through a spline, so in 61 there is the resulting curve.

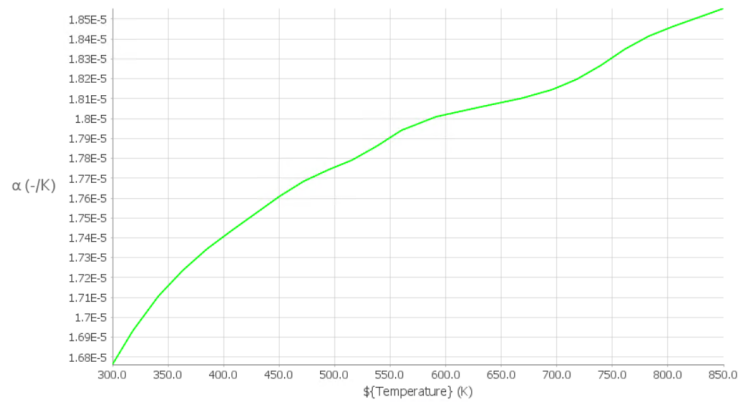


Figure 61: Visualization of the spline which approximates the α trend with temperature.

Specified Temperature

Solid Stress: which is a finite element method model, to work, it needs a **Material law** model in turn, which has been defined by the following models:

Material Stiffness: for this problem linear elasticity is assumed.

Linear Elastic Material Models: isotropic linear elasticity is chosen.

Thermal Expansion

Steel The models chosen are the following:

Space: three dimensional

Time: steady

Material: solid

Specified Temperature

Solid Stress: which is a finite element method model, to work, it needs a **Material law** model in turn, which has been defined by the following models:

Material Stiffness: for this problem linear elasticity is assumed.

Linear Elastic Material Models: isotropic linear elasticity is chosen.

Thermal Expansion

4.2 Mesh characteristic

The chosen mesh is a tetrahedral one, the base size is chosen to be the same of the one of the thermo-fluid dynamics evaluations.

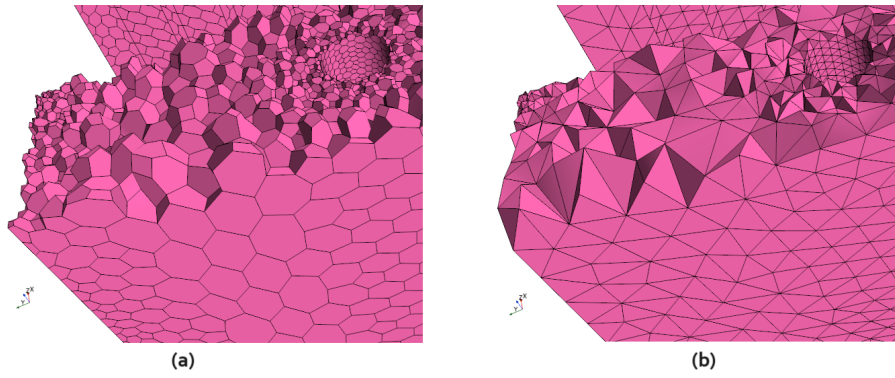


Figure 62: Visualization of polyhedral mesh (a) and tetrahedral mesh (b).

4.3 Panels and SFSS evaluations

4.3.1 Panels

Panels displacement is really important topic since it could affect the beam optics, that is the reason why it is important to have an idea of its magnitude.

temperature The temperature map evaluated in 3 refers to the discretization of the geometry obtained through the polyhedral mesh, and the result is obtained through finite volume method, while, in the thermo-mechanic evaluations is used a tetrahedral mesh, and finite element method. To make available the temperature map for the thermo-mechanical evaluations it is necessary to map the temperature and then interpolate the values in order to obtain a map of the values evaluated in the nodes of the thermo-mechanical assessment. This can be done exploiting a mapping Star CCM+ by indicating:

The property that has to be mapped, in this case, the temperature

The mesh over which the property was originally calculated

The destination mesh

As described in section 2.3, the 5 vertical panels have an horizontal part which connects them together, but the results of the 3rd simulation of the updated design, that should be the most accurate ones of all simulations, since these consider the entire SFSS geometry, were obtained considering a simplified geometry of the panels, shown in figure 51(c). To let the software automatically extrapolate the temperature map, over these parts gives a result which is very far from the reality, as seen in figure 63, since it is evidently different from an expected temperature distribution, that would have been more like the one shown in figure 46 (result of the 1st simulation of the upgraded design).

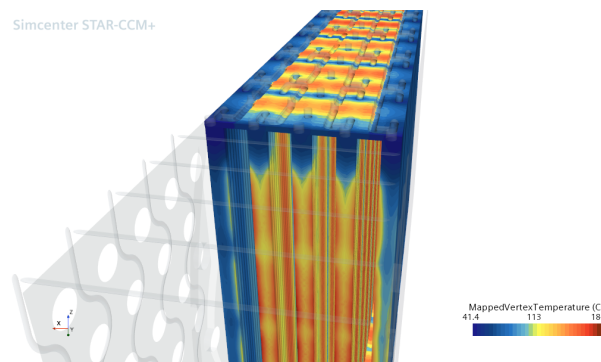


Figure 63: Star CCM+ temperature extrapolation, over the missing part of panel's CAD 3rd simulation of the updated design.

Therefore, the temperature distribution considered was just the one of the 1st simulation of the upgraded design, reported in figure 64 ,

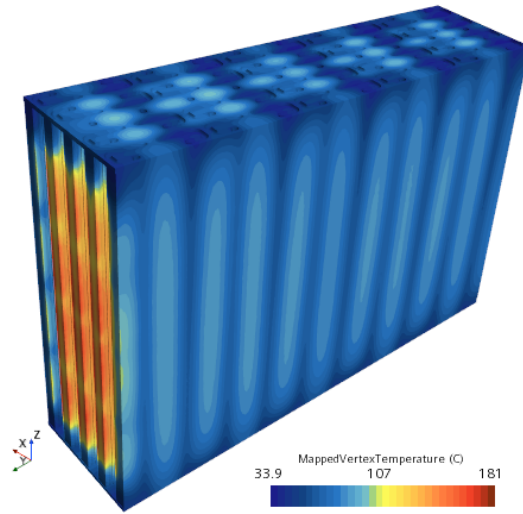


Figure 64: Temperature map on the panels only, according to the results of the simulation A.2.

Mechanical constraints To perform the evaluation of the effect of temperature on the displacement it is important to consider an appropriate set of boundary conditions.

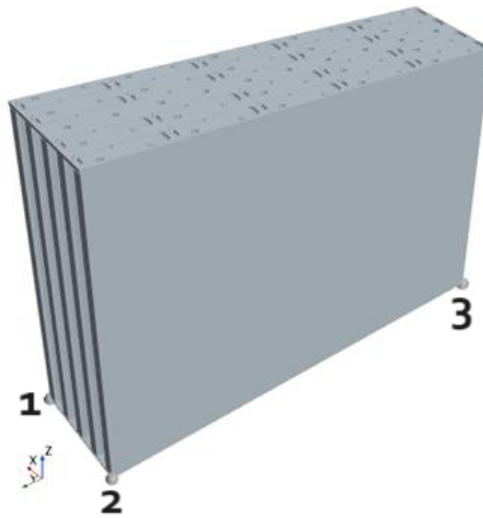


Figure 65: Constrained point of panels geometry.

Referring to points shown in figure 65, the employed constraints are the following:

1. Blocked along Y

2. Fixed
3. Blocked along Z

Results In figure 66 it is shown how the panels displace if subjected to the thermal load, according to this calculation, the maximum displacement should be around 4mm.

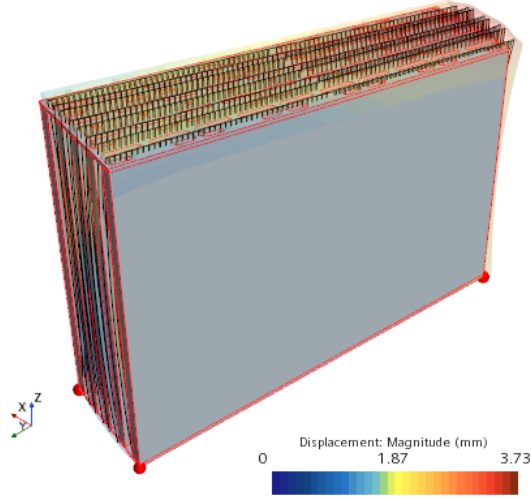


Figure 66: Result of the thermo-mechanical evaluation of the displacement.

The von Mises stress represents the magnitude of the deviatoric stress (which quantifies the distortion induced by externally applied forces):

$$\sigma_{vm} = \sqrt{\frac{1}{2}((s_1 - s_2)^2 + (s_1 - s_3)^2 + (s_2 - s_3)^2)} \quad (5)$$

where:

s_1, s_2, s_3 principal stresses of the point. At any point in the solid, there are always three planes, called principal planes, on which the shear stress (that is, the tangential component of the stress vector) is zero, the normal stresses of these planes are the principal stresses

To avoid yielding of the material it has to be satisfied:

$$\sigma_{vm} < \sigma_{Yelding} \quad (6)$$

In Star CCM+ it is possible to get a Von Mises Stress map over the investigated component, the result is shown in figure 67. It is observable that the largest part of the element undergoes a stress which is $\leq 200MPa$.

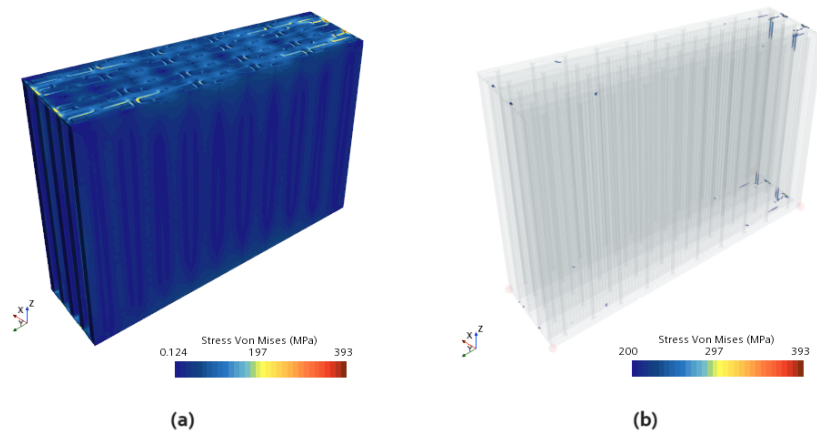


Figure 67: Result of the thermo-mechanical evaluation of the Von Mises Stress. In (a), there is an overview, in (b) the most loaded parts can be visualized.

To avoid yielding of the structure the maximum stress should be lower than the yield strength of CuCrZr which is between 60-570 MPa according to [23], the range is so wide since the properties of a material depends also on the way it is fabricated, here a SACwA treatment is assumed. If the results reported in [40] are taken as a reference, it can be observed in figure 68 that the largest part of the element should withstand the stress.

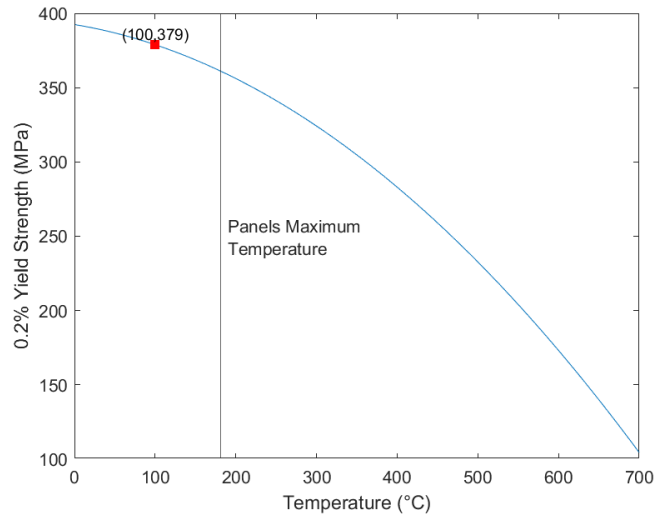


Figure 68: Yield Strength trend with temperature from [40], maximum temperature in panels is also reported.

The areas with the highest temperature undergo a stress well below their yielding. The areas shown in figure 67(b) are the ones whose stress is $\geq 200\text{MPa}$, if those are compared with the temperature map as shown in figure 69, it can be possible to notice that the temperature of most loaded parts could be, in some points close to $\sim 100^\circ\text{C}$.

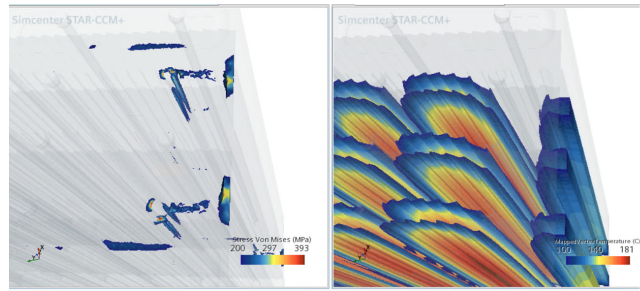


Figure 69: Comparison between von Mises Stresses and temperature maps.

From the point highlighted in figure 68 it is known that:

$$\sigma_{Y_{eld}@100^{\circ}C} \sim 379MPa \quad (7)$$

$$\sigma_{vmMAX} = 393MPa > \sigma_{Y_{eld}@100^{\circ}C} \sim 379MPa \quad (8)$$

Which means that, in the case considered, there is the possibility to have some sort of yield in some points of the structure. Here the thermo mechanic evaluations over the SFSS are presented. The overall procedure is similar to the one followed the one described in section 4.3.1.

temperature The temperature map considered in this phase is the one obtained by Simulation C.2, shown in figure 53.

mechanical constraints Constrained points set is really similar to the one described for panels, these are visualized in figure 70.

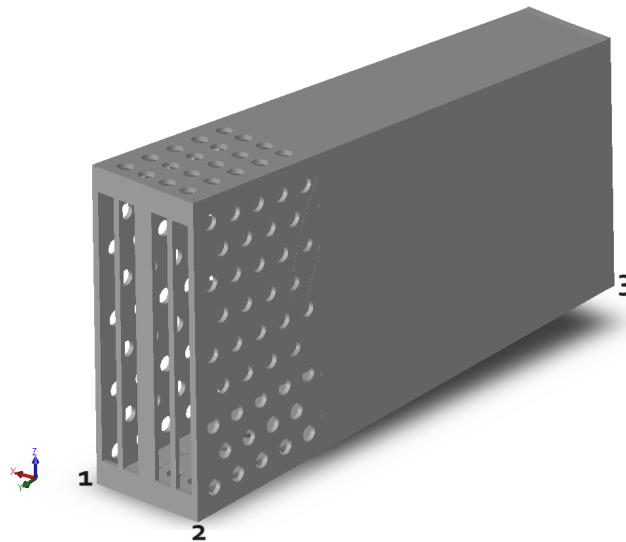


Figure 70: Constrained points of SFSS.

1. Blocked along Y

2. Fixed
3. Blocked along z

Results In this paragraph both the displacement and the stress are visualized in figure 71 and 72. According to the computed results, the maximum displacement should be around 3mm while the maximum stress around 961 MPa

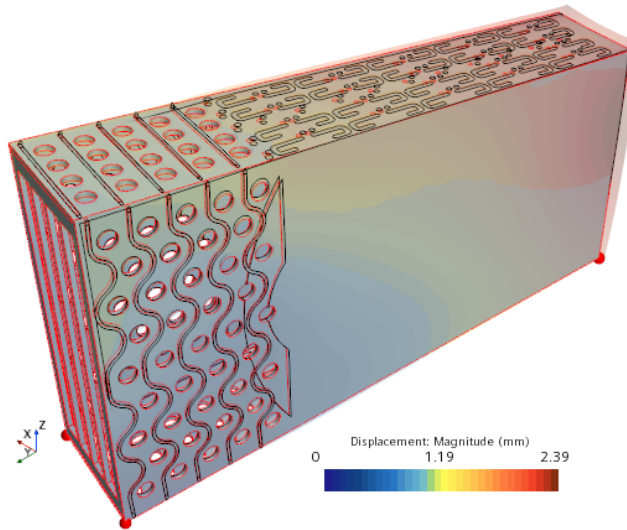


Figure 71: Displacement of SFSS

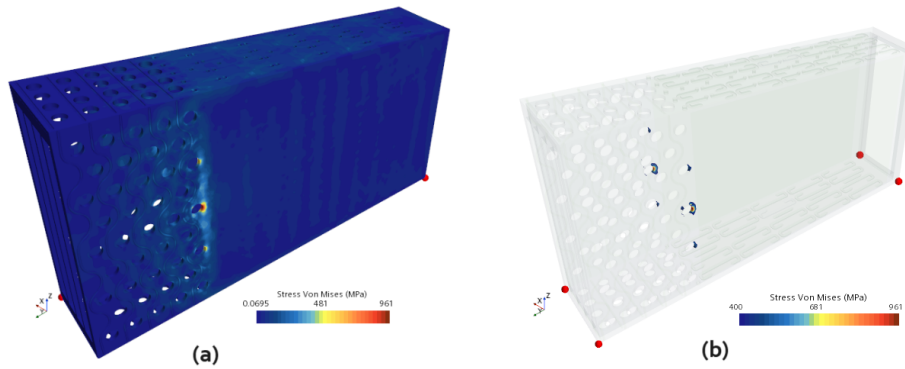


Figure 72: Result of the thermo-mechanical evaluation of the von Mises Stress of SFSS. In (a) there is an overview, in (b) the most loaded parts can be visualized.

The SS400 steel of which this component should be made of is named after the steel Japanese standard, and is really similar to the European S275JR [?], exhibit the following trend of yield strength with temperature:

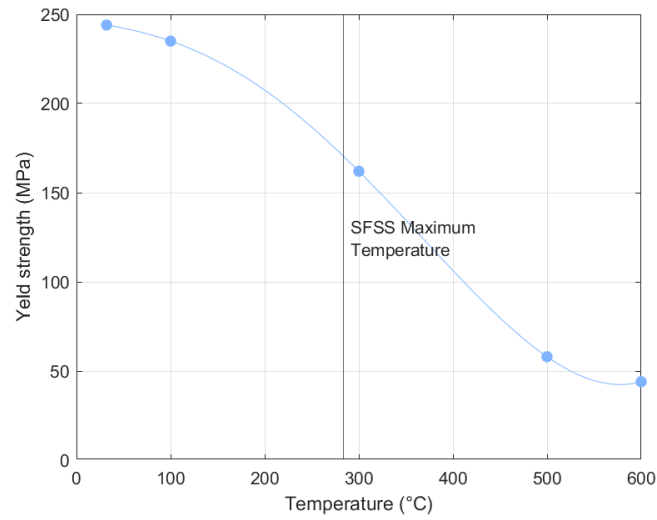


Figure 73: Yield strength trend with temperature, interpolation of data taken from [36].

Unlike the panels case reported in section 4.3.1, in this situation, the regions in which the temperature is the highest correspond with the ones in which the stress are the highest too. From [36] is taken the value of ultimate tensile stress at ambient temperature: $\sigma_{UTS} = 425MPa$, this value will decrease with temperature as well, thus the stress wouldn't withstandable, therefore the design 3 described in section 3.5 could be a solution for this issue.

5 Conclusions

The results of the analysis highlight that the pressure drop of 0.4 bar is fully compatible with the constraints. From the thermal-hydraulic point of view, after introducing in 2023 the spiral tape in the LEEs as a turbulence promoter, the design of the neutralizer is robust: the maximum fluid temperature is now lower than 150 °C, well below the saturation temperature of 212 °C, and the peak CuCrZr temperature, again in the LEEs, is 204 °C. This temperature is very close to 200 °C, the maximum temperature advisable to prevent ageing or recrystallization of the material. A higher hot spot temperature of 285 °C is computed on the surface of the SFSS, but the steel should be able to withstand it. The thermo-mechanical evaluation pointed out some issues, surely the evaluation should be carried out also on the latest version of the design to assess if the structure can withstand thermal loads avoiding unacceptable stresses.

References

- [1] Nuclear binding energy curve, 2023. https://en.wikipedia.org/wiki/Nuclear_binding_energy [Accessed: January 2024].
- [2] R Agnello, M Barbisan, R Pasqualotto, A Pimazzoni, C Poggi, E Sartori, and G Serianni. Measurement of stripping losses in the negative ion source spider. *Fusion Engineering and Design*, 186:113350, 2023.
- [3] P Agostinetti, E Benedetti, R Bonifetto, M Bonesso, M Cavenago, S Dal Bello, M Dalla Palma, D D'Ambrosio, R Dima, G Favero, et al. Improved conceptual design of the beamline for the dtt neutral beam injector. *IEEE Transactions on Plasma Science*, 50(11):4027–4032, 2022.
- [4] Piero Agostinetti. "Neutralizer_with_CSS_Sept22nd2023_fluid+solid.stp" and "Neutralizer_with_CSS_Sept22nd2023_only_fluid.stp", 2023.
- [5] Piero Agostinetti, Eugenio Benedetti, Tommaso Bolzonella, Massimiliano Bonesso, Irene Casiraghi, Razvan Dima, Giacomo Favero, Alberto Ferro, Marco Gobbin, Gustavo Granucci, et al. Conceptual design of the beamline for the dtt neutral beam injector following a double beam source design approach. *Plasma and Fusion Research*, 16:2405080–2405080, 2021.
- [6] John D Anderson Jr. Computational fluid dynamics-an engineering tool. *ASME Numerical/Laboratory Computer Methods in Fluid Mechanics*, pages 200–208, 1976.
- [7] Robert Arnoux. Hotter than the sun, 2014. <https://www.iter.org/mag/2/18> [Accessed: (2024)].
- [8] Elin M Carson and John R Watson. Undergraduate students' understandings of entropy and gibbs free energy. *University Chemistry Education*, 6(1):4–12, 2002.
- [9] Inc CiteDrive. The iter story, 2024. <https://www.iter.org/proj/ITERHistory> [Accessed: (2024)].
- [10] RFX consortium. La configurazione stellarator (italian). <https://www.igi.cnr.it/ricerca/negative-ion-neutral-beam-injection/la-configurazione-stellaretor> [Accessed: (2024)].
- [11] JR Cooper and RB Dooley. Revised release on the iapws industrial formulation 1997 for the thermodynamic properties of water and steam. *The International Association for the Properties of Water and Steam*, 1:48, 2007.
- [12] J Dietz and The Iter Joint Central Team. The iter fusion experiment. *Vacuum*, 47(6):911–918, 1996. Proceedings of the 13th International Vacuum Congress and the 9th International Conference on Solid Surfaces.
- [13] ENEA. Dtt divertor tokamak test facility project proposal, 2015.
- [14] ENEA. Divertor tokamak test facility – interim design report, 2019.
- [15] Eurofusion. Demonstration power plant demo, 2024. <https://euro-fusion.org/programme/demo/> [Accessed: January 2024].

- [16] Alberto Ferro, Francesco Lucchini, Piero Agostinetti, Daniele Ratti, Gustavo Granucci, Afra Romano, Roberto Romano, Antonio Cucchiaro, and Alessandro Princiotta. Conceptual design of the power supplies for dtt neutral beam injector. *Fusion Engineering and Design*, 169:112624, 2021.
- [17] Alberto Ferro, Loris Zanotto, Vanni Toigo, Luigi Rinaldi, Saverino Carrozza, Sandro Lazzari, Luca Sita, Alessandro Morato, Giuseppe Taddia, Daniel Gutierrez, et al. Manufacturing, installation, and commissioning of the residual ion dump power supply for mitica experiment. *IEEE Transactions on Plasma Science*, 48(6):1572–1578, 2020.
- [18] D. A. Gorissen. *Natuur Techniek*.
- [19] Raphael Gutser. Experiments and simulations for the dynamics of cesium in negative hydrogen ion sources for iter n-nbi. 2010.
- [20] C Hopf, G Starnella, N Den Harder, and U Fantz. Neutral beam injection for fusion reactors: Technological constraints versus functional requirements. *Nuclear Fusion*, 61(10):106032, 2021.
- [21] IEA. World gross electricity production by source, 2019.
- [22] IEA. Electricity market report 2023, 2023.
- [23] European Copper Institute. Cucr1zr data sheet, 2018.
- [24] Boštjan Končar, Domen Ovtar, Oriol Costa Garrido, and Piero Agostinetti. Calorimeter conceptual design for neutral beam injector of dtt-cfd optimisation and thermal stress analysis. *Fusion Engineering and Design*, 170:112469, 2021.
- [25] J Mlynář et al. Focus on: Jet the european centre of fusion research. *EFDA website*, 2007.
- [26] Jerome Pamela. The physics of production, acceleration and neutralization of large negative ion beams. *Plasma Physics and Controlled Fusion*, 37(11A):A325, 1995.
- [27] Padma Shukla and Alexandr Kendl. A brief hystory of controlled thermonuclear fusion. In *AIP Conference Proceedings*, volume 1445, pages 1–1. American Institute of Physics, 2011.
- [28] Siemens Digital Industries Software. Simcenter STAR-CCM+ User Guide v. 2022.1, Siemens 2022.
- [29] Johan Svensson, Roland Gårdhagen, Einar Heiberg, Tino Ebbers, Dan Loyd, Toste Lanne, and Matts Karlsson. Feasibility of patient specific aortic blood flow cfd simulation. volume 9, pages 257–63, 02 2006.
- [30] RFX Team. "Heat_load_NEU_[...].deuterium.csv" and "Heat_load_NEU_[...].elec.csv", for each LEE and panel side, 2023.
- [31] RFX Team, 2024.
- [32] Xavier Litaudon Carlos Hidalgo Darren McDonald Hartmut Zohm Eberhard Diegele Anton Möslang Kai Nordlund Gianfranco Federici Piergiorgio

Sonato Duarte Borba Per Helander Tony Donn , William Morris. European research roadmap to the realisation of fusion energy, long version, 2018.

- [33] Tutor. -, 2010.
- [34] Fabio Veronese, Piero Agostinetti, Giuseppe Calabr , Flavio Crisanti, Pierluigi Fanelli, Riccardo Lombroni, and Andrea Murari. Comparison among possible design solutions for the stray field shielding system of the dtt neutral beam injector. *Journal of Instrumentation*, 18(06):C06018, 2023.
- [35] Fabio Veronese, Piero Agostinetti, Andrea Murari, and Adriano Pepato. Performance optimization of the electrostatic accelerator for dtt neutral beam injector. *IEEE Transactions on Plasma Science*, 50(11):4033–4038, 2022.
- [36] Gia Hai Vuong, Nguyen Thi Hong Minh, and Nguyen Duc Toan. Mechanical properties of ss400 steel plate at elevated temperatures. *Applied Mechanics and Materials*, 889:51–57, 2019.
- [37] John Wesson and David J Campbell. *Tokamaks*, volume 149. Oxford university press, 2011.
- [38] Hiroshi Yamada. *Nuclear Fusion*, pages 1–45. Springer New York, New York, NY, 2020.
- [39] Jeong-Ha You. Copper matrix composites as heat sink materials for water-cooled divertor target. *Nuclear Materials and Energy*, 5:7–18, 2015.
- [40] Kuo Zhang, Ermile Gaganidze, and Michael Gorley. Development of the material property handbook and database of cuczr. *Fusion Engineering and Design*, 144:148–153, 2019.